

Molecular hydrogen in the $z_{\text{abs}} = 2.66$ damped Lyman- α absorber towards Q J 0643–5041 $\star, \star\star, \star\star\star$

Physical conditions and limits on the cosmological variation of the proton-to-electron mass ratio

D. Albornoz Vásquez¹, H. Rahmani^{2,3}, P. Noterdaeme¹, P. Petitjean¹, R. Srianand², and C. Ledoux⁴

¹ Institut d'Astrophysique de Paris, UMR 7095 CNRS, Université Pierre et Marie Curie, 98bis boulevard Arago, 75014 Paris, France
e-mail: danalbornoz@gmail.com

² Inter-University Centre for Astronomy and Astrophysics, Post Bag 4, Ganeshkhind, 411 007 Pune, India

³ School of Astronomy, Institute for Research in Fundamental Sciences (IPM), PO Box 19395-5531 Tehran, Iran

⁴ European Southern Observatory, Alonso de Córdova 3107, Casilla 19001, Vitacura, Santiago, Chile

Received 26 August 2013 / Accepted 31 October 2013

ABSTRACT

Context. Molecular hydrogen in the interstellar medium (ISM) of high-redshift galaxies can be detected directly from its UV absorption imprinted in the spectrum of background quasars. Associated absorption from H I and metals allow for the study of the chemical enrichment of the gas, while the analysis of excited species and molecules make it possible to infer the physical state of the ISM gas. In addition, given the numerous H₂ lines usually detected, these absorption systems are unique tools to constrain the cosmological variation of the proton-to-electron mass ratio, μ .

Aims. We intend to study the chemical and physical state of the gas in the H₂-bearing cloud at $z_{\text{abs}} = 2.658601$ towards the quasar Q J 0643–5041 ($z_{\text{em}} = 3.09$) and to derive a useful constraint on the variation of μ .

Methods. We use high signal-to-noise ratio, high-resolution VLT-UVES data of Q J 0643–5041 amounting to a total of more than 23 h exposure time and fit the H I, metals, and H₂ absorption features with multiple-component Voigt profiles. We study the relative populations of H₂ rotational levels and the fine-structure excitation of neutral carbon to determine the physical conditions in the H₂-bearing cloud.

Results. We find some evidence for part of the quasar broad-line emission region not being fully covered by the H₂-bearing cloud. We measure a total neutral hydrogen column density of $\log N(\text{H I})(\text{cm}^{-2}) = 21.03 \pm 0.08$. Molecular hydrogen is detected in several rotational levels, possibly up to $J = 7$, in a single component. The corresponding molecular fraction is $\log f = -2.19^{+0.07}_{-0.08}$, where $f = 2N(\text{H}_2)/(2N(\text{H}_2) + N(\text{H I}))$. The H₂ Doppler parameter is of the order of 1.5 km s^{-1} for $J = 0, 1$, and 2 and larger for $J > 2$. The molecular component has a kinetic temperature of $T_{\text{kin}} \approx 80 \text{ K}$, which yields a mean thermal velocity of $\sim 1 \text{ km s}^{-1}$, consistent with the Doppler broadening of the lines. The UV ambient flux is of the order of the mean ISM Galactic flux. We discuss the possible detection of HD and derive an upper limit of $\log N(\text{HD}) \lesssim 13.65 \pm 0.07$ leading to $\log \text{HD}/(2 \times \text{H}_2) \lesssim -5.19 \pm 0.07$, which is consistently lower than the primordial D/H ratio. Metals span $\sim 210 \text{ km s}^{-1}$ with $[\text{Zn}/\text{H}] = -0.91 \pm 0.09$ relative to solar, with iron depleted relative to zinc $[\text{Zn}/\text{Fe}] = 0.45 \pm 0.06$, and with the rare detection of copper. We follow the procedures used in our previous works to derive a constraint on the cosmological variation of μ , $\Delta\mu/\mu = (7.4 \pm 4.3_{\text{stat}} \pm 5.1_{\text{syst}}) \times 10^{-6}$.

Key words. galaxies: ISM – quasars: absorption lines – quasars: individual: Q J 0643-5041 – cosmology: observations

1. Introduction

Damped Lyman- α systems (DLA) are the spectral signature of large column densities of neutral hydrogen ($N(\text{H I}) \geq 2 \times 10^{20} \text{ cm}^{-2}$) located along the line of sight to bright background sources like quasi-stellar objects (QSOs) and gamma-ray bursts (GRBs).

* Based on data obtained with the Ultraviolet and Visual Echelle Spectrograph (UVES) at the European Southern Observatory Very Large Telescope (ESO-VLT), under program ID 080.A-0288(A) and archival data.

** Appendices are available in electronic form at <http://www.aanda.org>

*** Reduced spectra (FITS files) are only available at the CDS via anonymous ftp to cdsarc.u-strasbg.fr (130.79.128.5) or via <http://cdsarc.u-strasbg.fr/viz-bin/qcat?J/A+A/562/A88>

Because the involved H I column densities are similar to what is seen through galactic discs (e.g., Zwaan et al. 2005) and because of the presence of heavy elements (e.g., Pettini et al. 1997), DLAs are thought to be located close to galaxies and their circumgalactic media in which multi-phase gas is expected to be found. However, most of the gas producing DLAs is diffuse ($n < 0.1 \text{ cm}^{-3}$) and warm ($T > 3000 \text{ K}$) as evidenced by the scarcity of molecular (e.g., Petitjean et al. 2000) and 21 cm (Srianand et al. 2012) absorption lines. Indeed, direct measurements, via disentangling the turbulent and kinetic contributions to Doppler parameters of different species in single component absorption systems, report temperatures of the order of 10^4 K (Noterdaeme et al. 2012; Carswell et al. 2012). Such temperatures prevent molecular hydrogen formation on the surface of dust grains. In addition, ultra violet (UV) background radiation in DLA galaxies is large enough to photodissociate H₂ in

low-density gas clouds (Srianand et al. 2005b). Therefore, the average environment at DLA hosts is not favourable to the formation of H₂.

Consequently, H₂ is detected at $z > 1.8$ via Lyman- and Werner-band absorption lines in only about 10% of the DLAs (Noterdaeme et al. 2008a), down to molecular fractions of $f = 2N(\text{H}_2)/(2N(\text{H}_2) + N(\text{H I})) \simeq 1.0 \times 10^{-7}$ (Srianand et al. 2010). To our knowledge, 23 high- z H₂ detections in the line of sight of distant QSOs have been reported so far (Cui et al. 2005; Noterdaeme et al. 2008a and references therein; Srianand et al. 2008, 2010, 2012; Noterdaeme et al. 2010; Tumlinson et al. 2010; Jorgenson et al. 2010; Fynbo et al. 2011; Guimarães et al. 2012). Petitjean et al. (2006) show that selecting high-metallicity DLAs increases the probability of detecting H₂. This is the natural consequence of H₂ being more easily formed and shielded in dusty environments, as shown by the relation between the H₂ detection rate and the depletion factor (Ledoux et al. 2003) and that between the column densities of H₂ and that of metals missing from the gas phase (Noterdaeme et al. 2008a). The precise estimation of column densities of different H₂ rotational levels via Voigt profile fitting as well as the detection of excited states of neutral carbon allow for the study of the physical conditions of the gas (Srianand et al. 2005a; Noterdaeme et al. 2007a).

In the context of Grand Unified Theories, the fundamental parameter $\mu = m_p/m_e$, the proton-to-electron mass ratio could yield different values at distant space-time positions (for an up-to-date review on the variation of fundamental constants refer to Uzan 2011). Originally proposed by Thompson (1975), a probe of μ can be achieved in astrophysical absorbing systems by comparing the measured wavelengths of identified ro-vibrational transitions of molecules to their vacuum laboratory-established values. Relative shifts between different lines could be an evidence of $\mu_{\text{abs}} \neq \mu_{\text{lab}}$, where μ_{lab} is the laboratory measured value¹ and μ_{abs} is its value at the absorbing system.

This method has been used several times in the past (Varshalovich & Levshakov 1993; Cowie & Songaila 1995; Levshakov et al. 2002; Ivanchik et al. 2005; Reinhold et al. 2006; Ubachs et al. 2007; Thompson et al. 2009; Wendt & Molaro 2011, 2012; King et al. 2011; Rahmani et al. 2013). At present, measurements of $\Delta\mu/\mu$ using H₂ have been performed in seven H₂-bearing DLAs at $z > 2$ and suggest that $\Delta\mu/\mu < 10^{-5}$ at $2 < z < 3$. At $z < 1.0$, a stringent constraint on $\Delta\mu/\mu$ is obtained using inversion transitions of NH₃ and rotational molecular transitions (Murphy et al. 2008; Henkel et al. 2009; Kanekar 2011). The best reported limit using this technique is $\Delta\mu/\mu = (3.5 \pm 1.2) \times 10^{-7}$ (Kanekar 2011). Bagdonaite et al. (2013) obtained the strongest constraint till date of $\Delta\mu/\mu = (0.0 \pm 1.0) \times 10^{-7}$ at $z = 0.89$ using methanol transitions. Tight constraints have been obtained using 21-cm absorption in conjunction with UV metal lines and assuming all other constants have not changed: Rahmani et al. (2012) derived $\Delta\mu/\mu = (0.0 \pm 1.50) \times 10^{-6}$, using a sample of four 21 cm absorbers at $z < 1.3$, and Srianand et al. (2010) measured $\Delta\mu/\mu = (1.7 \pm 1.7) \times 10^{-6}$ at $z = 3.17$, using the 21-cm absorber towards J1337+3152.

In this work, we fit the H₂ absorption features to determine the physical conditions in the $z_{\text{abs}} = 2.6586$ DLA towards Q J0643–5041. We discuss the detection of HD and give an upper limit on the deuterium abundance in the molecular component. We present a critical analysis of the data. In particular, we search for any partial coverage of the QSO broad-line region by

the intervening cloud, and search with great care for systematic errors in wavelength calibration having an impact on the precise estimation of the absorbing wavelength λ_{obs} of all H₂ transitions. We make use of numerous H₂ transitions detected to derive a limit on $\Delta\mu/\mu$.

2. Observations and data processing

The detection of H₂ at $z_{\text{abs}} = 2.66$ towards Q J0643–5041 ($z_{\text{em}} = 3.09$) was first reported in Noterdaeme et al. (2008a). Several programs observed this quasar using both spectroscopic VLT-UVES arms (Dekker et al. 2000) in 2003 and 2004: 072.A-0442(A), aimed to study DLAs (PI S. López); 073.A-0071(A), aimed to search for H₂-bearing systems at high redshift (PI Ledoux); and 074.A-0201(A), aimed to constrain the variation of the fine-structure constant at high redshift using metal absorption lines (PI R. Srianand). The observers used a slit of 1.2 arcsec and a 2×2 -binned CCD, resulting in a spectral resolving power of $R \sim 40\,000$ or full width at half maximum ($FWHM$) = 7.5 km s⁻¹ in the blue arm and $R \sim 36\,000$, or $FWHM = 8.3$ km s⁻¹ in the red arm. These programs did not include attached ThAr lamp calibration exposures. We also use more recent (2007–2008) data, program ID 080.A-0228(A) aimed to constrain the cosmological variation of μ (PI Petitjean). A UVB spectrum derived from these observations is shown in Fig. 1. The settings for the exposures were a 1 arcsec slit and 2×2 binning of the CCD pixels, for a resolving power of $R \sim 45\,000$, or $FWHM = 6.7$ km s⁻¹ in the blue arm, and $R \sim 43\,000$, or $FWHM = 7.0$ km s⁻¹ in the red arm. We performed wavelength calibration with attached ThAr exposures. Here, we solely focused the data acquisition on H₂ transitions. Hence, the H₂ lines are apparent in all the observing data sets, while metal lines falling in the red arm ($\lambda > 4500$ Å) are observed only in the early observations. Blue arm exposures, relevant for detecting H₂ absorption lines, are listed in Table 1.

We reduced all the data using UVES Common Pipeline Library (CPL) data reduction pipeline release 5.3.11², using the optimal extraction method. We used 4th order polynomials to find the dispersion solutions. The number of suitable ThAr lines used for wavelength calibration was usually more than 700 and the rms error was found to be in the range 70–80 m s⁻¹ with zero average. However, this error reflects only the calibration error at the observed wavelengths of the ThAr lines that are used for wavelength calibration. Systematic errors affecting wavelength calibration should be measured with other techniques that will be discussed later in the paper. All the spectra are corrected for the motion of the observatory around the barycentre of the solar system. The velocity component of the observatory's barycentric motion towards the line of sight to the QSO was calculated at the exposure mid point. Conversion of air to vacuum wavelengths was performed using the formula given in Edlén (1966). We interpolate these spectra into a common wavelength array and generate the weighted mean combined spectrum, using the inverse square of error as the weight. This is the combined spectrum we use to study the physical condition of this absorption system.

To study of the variation of μ , we only consider those exposures that have the attached mode ThAr lamp calibration. We follow a more careful procedure to make a new combined spectrum from these exposures. We start from the final un-rebinned

¹ In the laboratory: $\mu_{\text{lab}} = m_p/m_e \simeq 1836.1526675(39)$ (Mohr & Taylor 2000).

² <http://www.eso.org/sci/facilities/paranal/instruments/uves/doc>

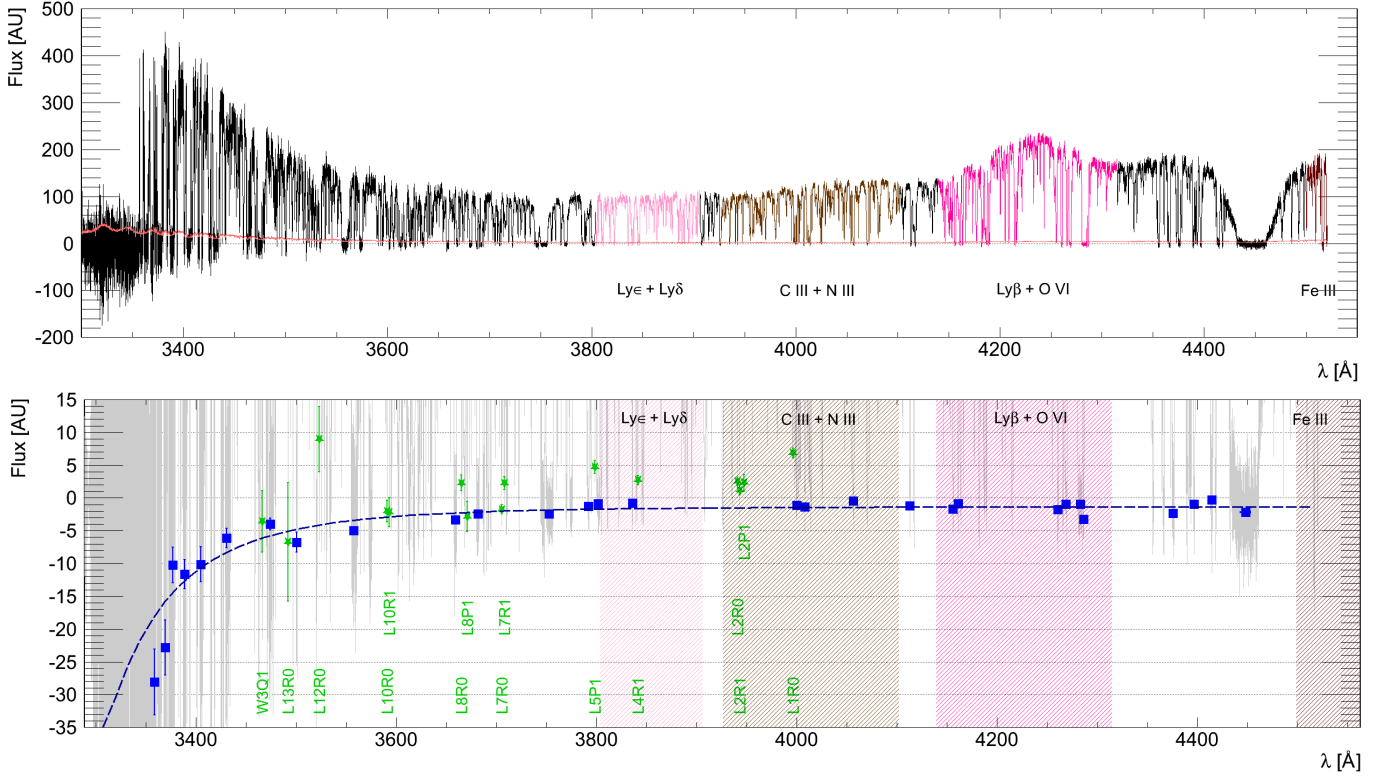


Fig. 1. *Top panel:* Q J0643–5041 spectrum obtained after combining the 15 exposures with central grating setting at 390 nm and attached ThAr lamp exposure for wavelength calibration. In colours, the broad-line emission line intervals as expected from the composite emission spectrum of quasars from [Vanden Berk et al. \(2001\)](#) at $z_{\text{em}} = 3.09$. *Bottom panel:* the median of the selected intervals from saturated Lyman- α forest absorption lines for the analysis of the zero level are shown in blue square points. The error bar on the flux is the error on the mean measured flux of the selected pixels. The dashed line is the fit to the medians taking the errors into account. Green star points represent the median level at the bottom of saturated and unblended H₂ lines. We compute error bars equivalent to those of blue points. We show the broad-line region expected extension as given in [Vanden Berk et al. \(2001\)](#) in shaded colours, and the flux measured in gray in the background.

Table 1. Summary of Q J0643–5041 exposures containing H₂ and HD absorption features at $z_{\text{abs}} \approx 2.6586$, using the blue arm of the Ultraviolet and Visual Echelle Spectrograph at ESO-VLT used for analysis in the present work.

#	Program ID	Date	Grating central wavelength [nm]	DIMM Seeing [arcsec] ^a	Airmass	Exposure time [s]	Wavelength calibration
1	073.A-0071(A)	17-09-2004	390	2.3 → 1.89	1.522 → 1.229	5500	...
2	073.A-0071(A)	18-09-2004	390	1.91 → 1.9	1.561 → 1.229	6000	...
3	073.A-0071(A)	19-09-2004	390	0.87 → 1.0	1.545 → 1.222	6000	...
4	074.A-0201(A)	09-10-2004	390	... → 0.6	1.316 → 1.143	5800	...
5	074.A-0201(A)	10-10-2004	390	... → 0.37	1.291 → 1.139	5500	...
6	080.A-0288(A)	11-12-2007	390	0.87 → ...	1.165 → 1.279	3725	ThAr attached
7	080.A-0288(A)	03-01-2008	390	1.04 → 0.91	1.182 → 1.122	3725	ThAr attached
8	080.A-0288(A)	04-01-2008	390	0.82 → 1.77	1.233 → 1.143	3725	ThAr attached
9	080.A-0288(A)	04-01-2008	390	1.3 → 1.66	1.140 → 1.113	3725	ThAr attached
10	080.A-0288(A)	04-01-2008	390	1.66 → 1.69	1.113 → 1.118	1389	ThAr attached
11	080.A-0288(A)	06-01-2008	390	1.24 → ...	1.128 → 1.113	2104	ThAr attached
12	080.A-0288(A)	06-01-2008	390	0.89 → 1.24	1.173 → 1.295	3725	ThAr attached
13	080.A-0288(A)	06-01-2008	390	1.1 → 1.08	1.311 → 1.545	3725	ThAr attached
14	080.A-0288(A)	07-01-2008	390	1.07 → 0.84	1.215 → 1.135	3725	ThAr attached
15	080.A-0288(A)	13-01-2008	390	0.69 → 1.0	1.347 → 1.201	3725	ThAr attached
16	080.A-0288(A)	16-01-2008	390	0.6 → 0.85	1.121 → 1.178	3725	ThAr attached
17	080.A-0288(A)	06-02-2008	390	... → ...	1.113 → 1.136	3725	ThAr attached
18	080.A-0288(A)	07-02-2008	390	0.8 → 0.9	1.125 → 1.190	3725	ThAr attached
19	080.A-0288(A)	09-02-2008	390	... → 0.8	1.113 → 1.145	3725	ThAr attached
20	080.A-0288(A)	10-02-2008	390	1.24 → 0.81	1.215 → 1.374	3725	ThAr attached
21	072.A-0442(A)	02-11-2003	437	2.16 → 1.65	1.251 → 1.153	3600	...

Notes. We used 42 other (red arm) exposures with grating central wavelengths of 564, 580, 760, and 850 nm were used for the fits of metallic absorption lines. ^(a) Some values were not measured (...).

extracted spectrum of each order produced by the CPL. We apply the CPL wavelength solution to each order and merge the orders by implementing a weighted mean in the overlapping regions. In the last step, we made use of a uniform wavelength array of step size of 2.0 km s^{-1} for all exposures. As a result, no further rebinning is required for spectrum combination. We fitted a continuum to each individual spectrum and generated a combined spectrum using a weighted mean. We further fit a lower order polynomial to adjust the continuum. This spectrum will be used for $\Delta\mu/\mu$ measurement. In Rahmani et al. (2013), we found this procedure to produce final combined spectrum consistent with that obtained using UVES_POPLER.

3. Residual zero-level flux: partial coverage?

Quasi-stellar objects are compact objects emitting an intrinsic and extremely luminous continuum flux. Broad emission lines seen in the spectra of QSOs are believed to originate from an extended region of $\sim\text{pc}$ size, the broad-line region (BLR). Balashev et al. (2011) reported that an intervening molecular cloud towards Q1232+082 covers only a fraction of the BLR, most probably because of its compact size. This results in a residual flux detected at the bottom of saturated spectral features associated with the neutral cloud at wavelengths that are coincident with the BLR emission.

Here, we search for a similar effect. For this, we estimate the residual flux at the bottom of saturated H_2 lines of the molecular cloud at $z_{\text{abs}} = 2.6586$ towards Q J0643–5041. We verify the instrumental zero flux level of the spectra first, bearing in mind that UVES is not flux calibrated. We estimate the residual flux at the bottom of saturated Lyman- α -forest lines, associated with large scale gas clouds in the intergalactic medium that are extended enough to cover the background source completely. We consider 29 sets of pixels defined by intervals in wavelengths close to the center of saturated Lyman- α -forest lines first, with no interference with H_2 transitions. The median flux value for each interval with its error is represented by blue points in the bottom panel of Fig. 1. We fit the observed distribution with a simple function of the wavelength, represented by the dotted line in the bottom panel of Fig. 1, and correct the systematic zero error by subtracting it from the flux.

We estimate the residual flux at the bottom of saturated H_2 transitions unblended with other absorption features. We normalise the flux and fit the H_2 system. For this analysis, all fitting parameters (redshift, column density, and Doppler parameter) of a given rotational level are tied for all lines. The fit shows that for some of the most saturated lines the flux measured at the bottom of the lines is clearly above the Voigt profile absorption model. We select the pixels where the model fit falls below 1% of the emitted flux and plot in green in the bottom panel of Fig. 1 the resulting median flux of such selected pixels. The measured flux at the bottom of saturated H_2 lines is systematically larger than that measured at the bottom of the Lyman- α forest saturated lines, in blue in the bottom panel in Fig. 1.

To establish whether this residual flux is due to partial coverage of the BLR, we attempt to measure the BLR emission. Unfortunately, because of the difference between emitting and absorbing redshifts, only a few saturated H_2 lines fall on top of broad emission lines of C III, N III, Lyman- δ , and Lyman- ϵ . As shown in the top panel of Fig. 1, the relative amplitude of these features with respect to the total emitted flux is very small. Nonetheless, we estimate the Q J0643–5041 continuum emission alone by ignoring the wavelength intervals where the

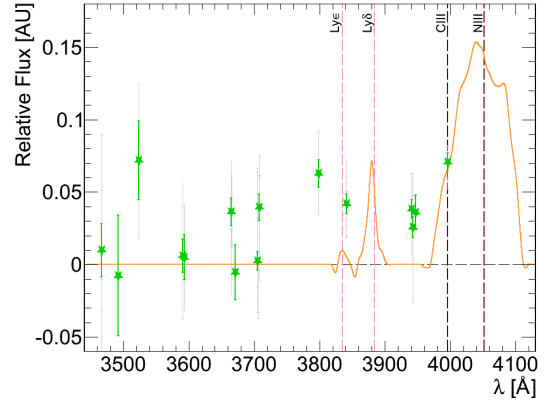


Fig. 2. Fraction of emitted flux attributed to the broad-line region associated with Q J0643–5041 is drawn in solid line. We indicate the position of the emission lines at $z_{\text{em}} = 3.09$. Pixels corresponding to saturated H_2 transitions are shown in gray, and in green star points their median at each selected line position.

BLR emission is expected as defined in Vanden Berk et al. (2001) (coloured and shaded regions in Fig. 1). After subtracting this continuum contribution, we are left with the relative BLR emission, which is plotted in solid line in Fig. 2.

In this figure, we see that green points, representing the residual flux at the bottom of H_2 saturated lines, are systematically above the 1% level. Around the BLR emitting region the effect is possibly larger. Note that the variation does not follow the BLR emission fraction exactly as is also the case in Balashev et al. (2011). The distribution of these points shows roughly two behaviours. Below $\sim 3750 \text{ \AA}$, the points are distributed around $\approx 1\%$, and above $\sim 3750 \text{ \AA}$, they are distributed around $\approx 5\%$, with altogether larger dispersion towards the blue where the signal-to-noise ratio (S/N) is lower. A closer look at the distribution of these points shows that there are two distributions, one peaked at zero flux as it should be for a full absorption, and another peaked at $\approx 4\%$ of the total flux. While all points, on the BLR emission lines or not, contribute to the $\approx 4\%$ peak, only those not associated with BLR emission peak at zero flux. It is therefore possible that part of the BLR is not covered. The only absorption line located on top of an important broad emission line is L1R0 falling on top of C III (see Fig. 2). It has the highest residual of all absorption lines. Actually, the residual flux matches the relative flux attributed to C III exactly, however, this is probably a chance coincidence.

In conclusion, we can say that, although not striking, there is at least weak evidence for the BLR to be partly covered by the H_2 bearing cloud (see also Sect. 5.4). A higher S/N spectrum would be required to confirm or refute the partial coverage. The effect being poorly determined and globally small, we do not attempt to take it into account when fitting H_2 lines with Voigt profiles. In particular, the saturated lines we use can be fitted in the wings of the absorption profile where partial coverage does not have any impact. Moreover, metal profiles are dominated by strong and saturated components stemming from diffuse extended gas.

4. Fit of the absorption profiles

We proceed by studying the various absorption lines associated with the DLA, fitting Voigt profiles with the Voigt profile fitting program (VPFIT) 10.0³. The reference absorption redshift

³ <http://www.ast.cam.ac.uk/~rfc/vpfit.html>

Table 2. Metal components in the absorbing system at $z_{\text{abs}} = 2.659$ towards Q J0643–5041 obtained with multi-component fit using VPFIT.

#	Δv [km s ⁻¹]	b [km s ⁻¹]	Zn II log(N) [cm ⁻²]	S II log(N) [cm ⁻²]	Si II log(N) [cm ⁻²]	Cr II log(N) [cm ⁻²]	Fe II log(N) [cm ⁻²]	Ni II log(N) [cm ⁻²]	Cu II log(N) [cm ⁻²]
1	-122.9 ± 0.1	8.5 ± 0.2	11.70 ± 0.11	13.80 ± 0.18	13.10 ± 0.01	12.37 ± 0.14	12.54 ± 0.03	12.05 ± 0.17	...
2	-100.0 ± 1.1	3.7 ± 0.5	11.28 ± 0.23 ^a	13.49 ± 0.29	12.99 ± 0.21	11.61 ± 0.82	12.65 ± 0.21	11.78 ± 0.40	...
3	-96.0 ± 0.4	2.8 ± 0.5	13.33 ± 0.10	11.89 ± 0.42	12.99 ± 0.10	11.83 ± 0.36	...
4	-87.4 ± 1.1	5.2 ± 1.1	11.77 ± 0.10	13.16 ± 0.65	13.08 ± 0.07	...	12.68 ± 0.08	11.94 ± 0.21	...
5	-77.1 ± 0.5	2.4 ± 0.6	11.29 ± 0.26 ^a	13.82 ± 0.19	12.73 ± 0.11	12.07 ± 0.22	12.47 ± 0.08
6	-68.8 ± 1.2	5.3 ± 2.0	11.14 ± 0.39 ^a	13.73 ± 0.27	12.78 ± 0.23	11.74 ± 0.55	12.30 ± 0.30	11.94 ± 0.26	...
7	-56.5 ± 3.9	8.7 ± 5.5	...	13.55 ± 0.53	12.95 ± 0.42	12.17 ± 0.44	12.61 ± 0.41	12.03 ± 0.39	...
8	-45.9 ± 1.6	8.3 ± 1.3	11.37 ± 0.27 ^a	13.25 ± 0.90	13.26 ± 0.17	12.44 ± 0.20	12.91 ± 0.17	11.76 ± 0.62	...
9	-27.7 ± 0.6	5.0 ± 0.7	11.17 ± 0.37 ^a	13.77 ± 0.21	13.33 ± 0.08	12.10 ± 0.18	12.92 ± 0.08	12.17 ± 0.10	...
10	-20.6 ± 0.3	2.4 ± 0.3	10.71 ± 0.97 ^a	13.50 ± 0.39	13.82 ± 0.06	11.95 ± 0.24	13.24 ± 0.05	12.06 ± 0.13	...
11	-11.9 ± 0.7	8.3 ± 2.2	10.93 ± 0.79 ^a	13.85 ± 0.21	13.64 ± 0.10	12.18 ± 0.19	13.15 ± 0.10	12.21 ± 0.13	11.62 ± 0.13
12	0.7 ± 0.1	2.9 ± 0.1	12.10 ± 0.06	14.57 ± 0.07	14.84 ± 0.02	12.53 ± 0.06	14.39 ± 0.03	12.96 ± 0.02	11.44 ± 0.12
13	17.0 ± 0.5	7.1 ± 0.5	11.48 ± 0.31	14.37 ± 0.08	14.76 ± 0.04	12.71 ± 0.07	14.43 ± 0.04	13.00 ± 0.04	11.70 ± 0.09
14	25.2 ± 0.7	2.7 ± 0.5	...	14.27 ± 0.11	14.11 ± 0.15	12.34 ± 0.12	13.90 ± 0.12	12.56 ± 0.10	11.19 ± 0.23
15	34.5 ± 0.7	3.9 ± 1.4	10.87 ± 0.85 ^a	13.83 ± 0.16	13.68 ± 0.17	12.21 ± 0.14	13.35 ± 0.15	12.10 ± 0.17	11.38 ± 0.15
16	48.4 ± 1.1	7.2 ± 1.0	11.80 ± 0.17	14.35 ± 0.14	14.83 ± 0.09	12.90 ± 0.09	14.48 ± 0.10	13.15 ± 0.09	11.64 ± 0.13
17	56.7 ± 0.6	5.3 ± 1.0	11.63 ± 0.21	14.54 ± 0.14	14.75 ± 0.12	12.57 ± 0.25	14.29 ± 0.15	13.00 ± 0.15	10.66 ± 1.35
18	66.7 ± 2.5	10.5 ± 1.9	...	14.34 ± 0.22	13.88 ± 0.23	12.69 ± 0.30	13.51 ± 0.17	12.86 ± 0.17	11.56 ± 0.17
19	67.1 ± 0.5	4.2 ± 0.5	11.67 ± 0.19	...	14.46 ± 0.07	12.11 ± 0.57	14.18 ± 0.05	12.59 ± 0.11	...
20	72.5 ± 4.8	2.4 ± 1.6	11.18 ± 0.47 ^a	13.90 ± 0.28	13.59 ± 0.24	8.91 ± 10.64	...
21	85.6 ± 0.9	5.6 ± 0.7	10.76 ± 1.44 ^a	13.75 ± 0.22	13.10 ± 0.08	12.49 ± 0.10	12.63 ± 0.08	11.81 ± 0.19	11.18 ± 0.22
Σ			12.75 ± 0.05	15.35 ± 0.05	15.52 ± 0.03	13.66 ± 0.06	15.14 ± 0.04	13.84 ± 0.04	12.41 ± 0.06
$\left[\frac{X}{H}\right]$			-0.91 ± 0.09	-0.87 ± 0.09	-1.05 ± 0.09	-1.02 ± 0.10	-1.36 ± 0.09	-1.41 ± 0.09	-0.88 ± 0.10
$\left[\frac{X}{Zn}\right]$				0.03 ± 0.07	-0.14 ± 0.06	-0.11 ± 0.07	-0.45 ± 0.06	-0.50 ± 0.06	0.03 ± 0.08
$\left[\frac{X}{S}\right]$			-0.03 ± 0.07		-0.18 ± 0.06	-0.14 ± 0.07	-0.49 ± 0.06	-0.53 ± 0.06	-0.01 ± 0.07

Notes. Doppler parameters are those of Si II. ^(a) Column density below 3 σ detection.

(defining the origin of our adopted velocity scale) is set to the position of the detected C I component, i.e., $z_{\text{abs}} = 2.65859(7)$.

4.1. H I content

To determine the H I absorption profile, we checked the structure of the absorption profiles of other elements thought to be associated with H I such as C II and O I. Both of these elements feature a multi-component saturated pattern spanning about 200 km s⁻¹ (see Fig. A.11). It is, therefore, difficult to have a precise H I absorption decomposition, hence to have a good estimate of the H I column density at the position of the molecular cloud. A main component is fixed at $z_{\text{abs}} = 2.65859(7)$, and the fit to Lyman- α and Lyman- β gives $N_{\text{main}}(\text{H I}) = 10^{21.03 \pm 0.08} \text{ cm}^{-2}$, which is consistent with all other H I transitions (see Fig. A.1). The other nine components (with $N_{\text{other}}(\text{H I}) < 10^{17.3} \text{ cm}^{-2}$) were added to match the H I profile down to Lyman-7.

4.2. Metal content

Low ionisation species, Fe II, Cr II, Si II, Zn II, S II, Mg I, P II, Cu II, and Ni II, are detected in a multi-component absorption pattern spanning about $\sim 210 \text{ km s}^{-1}$, with roughly a 125 km s^{-1} extension towards the blue and 85 km s^{-1} towards the red, with respect to the carbon and molecular component at $z = 2.65859(7)$. The absorption profiles are fitted with 21 velocity components. After a first guess is obtained, we perform a fit with tied redshifts and Doppler parameters between different species. The latter is taken as the combination of a kinematical term for a fixed temperature of 10^4 K and a turbulent term, which is the same for all species. The resulting profile can be seen in Fig. A.11 and the parameters of the fit are given in Table 2. The turbulent term is the

major component of the Doppler parameters. We caution that the Zn II column densities over the range $v = -90, -25 \text{ km s}^{-1}$ are probably overestimated as they appear relatively strong compared to other species. This is likely due to contaminations from telluric features and sky line residuals. Taking the noise in the portions of spectra relevant to Zn II into account, the 3 σ detection limit is at $\log N \simeq 11.47$, showing that the blue components of Zn II are below the noise level. We note that using the 3 σ upper-limits instead of the fitted column densities has negligible influence on the derived total column density of zinc. Interestingly, we detect weak, but significant Cu II $\lambda 1358$ absorption, consistently with non-detection of the weaker Cu II $\lambda 1367$. The profile follows that of other species well and we measure a total column density of $\log N(\text{Cu II}) = 12.41 \pm 0.06$. To our knowledge, this is only the second detection of copper in a DLA (see Kulkarni et al. 2012).

Highly ionised species, C IV, Si IV, and Al III, are detected with a broad profile with maximum optical depth at $\sim 45 \text{ km s}^{-1}$ towards the red from the molecular component (corresponding to components number 16 and 12 respectively, see Table 2). The latter component is quite weak compared to the strongest component. Highly ionised species are, hence, much more present redwards of the molecular component. Voigt profile fits to these elements are displayed in Fig. A.10.

4.3. Molecular hydrogen

Absorption features of molecular hydrogen fall exclusively in the blue arm. We use the ThAr attached wavelength calibrated spectrum to fit the molecular transition lines with Voigt profiles.

Table 3. H₂, C I, and C II* column densities in the $z_{\text{abs}} = 2.6586$ H₂-bearing cloud towards Q J 0643–5041.

Transition	Δv^a [km s ⁻¹]	$\log(N)$ [cm ⁻²]	$\log(N_{\text{lim}})$ [cm ⁻²]	b [km s ⁻¹]
H ₂ ($J = 0$)	0.25 ± 0.08	18.22 ± 0.01	...	1.59 ± 1.10^d
H ₂ ($J = 1$)	0.25 ± 0.08	18.25 ± 0.01	...	1.39 ± 0.70^d
H ₂ ($J = 2$)	0.33 ± 0.08	16.62 ± 0.12	...	1.41 ± 0.29^d
H ₂ ($J = 3$)	0.33 ± 0.08	14.84 ± 0.05	...	2.14 ± 0.61^d
H ₂ ($J = 4$)	0.57 ± 0.25	13.94 ± 0.02	...	3.45 ± 1.01^d
H ₂ ($J = 5$)	0.25^b	13.86 ± 0.07	...	9.49 ± 2.37
H ₂ ($J = 6$)	0.25^b	13.40 ± 0.16	13.7	9.49^b
H ₂ ($J = 7$)	0.25^b	13.35 ± 0.13	13.5	9.49^b
C I	0 ± 0.25	12.57 ± 0.09	...	0.71 ± 0.29
C I*	0 ± 0.25^c	12.47 ± 0.06	...	0.71 ± 0.29^c
C I**	0 ± 0.25^c	11.48 ± 0.30	11.95	0.71 ± 0.29^c
C II*	0.82 ± 0.08	14.12 ± 0.04	...	1.30 ± 0.04

Notes. (a) Velocity relative to C I. (b) Fixed value. (c) Tied parameter. (d) Statistical spread rather than fit error.

Molecular hydrogen is detected in a single component for rotational levels $J = 0$ to 5. The Voigt profile fit is not always satisfactory, in particular for $J = 0$ and $J = 1$ saturated lines. As was already stated, there is often residual flux at the bottom of the saturated lines. The detection is secured for $J = 0$ to 5 with a reliable fit. For $J = 6$, the L4P6 and L5P6 are detected at the 1.7σ confidence level only. The 3σ level upper limit of the column density is $N(\text{H}_2, J = 6) \leq 10^{13.65} \text{ cm}^{-2}$. Regarding $J = 7$, the L5R7 is detected at the 2.1σ confidence level only. The 3σ column density upper limit is $N(\text{H}_2, J = 7) \leq 10^{13.51} \text{ cm}^{-2}$. Nonetheless, we perform a fit to these rotational levels with fixed Doppler parameter (to the value of the parameter of $J = 5$), which is in agreement with the upper limits. A summary of the fit to the H₂ lines is given in Table 3, while a selection of Voigt profile fits to the most isolated lines can be found in Figs. A.2–A.6.

The total column density is $N(\text{H}_2) = 10^{18.540 \pm 0.005} \text{ cm}^{-2}$ with 99% of this amount in the first two rotational levels. The molecular fraction $f = 2N(\text{H}_2)/(N(\text{H I}) + 2N(\text{H}_2))$ is therefore $\log f = -2.19^{+0.07}_{-0.08}$ when taking all atomic hydrogen into account. Since the atomic hydrogen column density at the position of the molecular cloud is probably lower than the total measured column density, we get $f \gtrsim 10^{-2.19}$. A molecular fraction of $\log f = -2.19$ is comparable to the average molecular fractions recorded in high redshift DLA systems with $\log f > -4.5$ (see Noterdaeme et al. 2008a) (with ten systems satisfying this condition, the mean is $\langle \log f \rangle \simeq -2.3$).

4.4. Deuterated molecular hydrogen

We study the best HD transitions available, normalising the flux locally and accounting for obvious contaminations. We select seven $J = 0$ transitions (L5R0, L7R0, L12R0, L13R0, W0R0, W3R0, and W4R0), and five $J = 1$ transitions (L2P1, L4P1, L7R1, L9P1, and W0R1). The spectral portions around these transitions are shown in Figs. A.7 and A.8 with an indicative Voigt profile model. Then we stacked these isolated spectra, weighting the transitions by the local S/N and by the oscillator strength of the transition. Finally, we compare this stack with a synthetic spectrum of the transitions with the same weights, and with redshift and Doppler parameters set to the H₂ $J = 0, 1$. The result is shown in Fig. 3. For $J = 0$ we

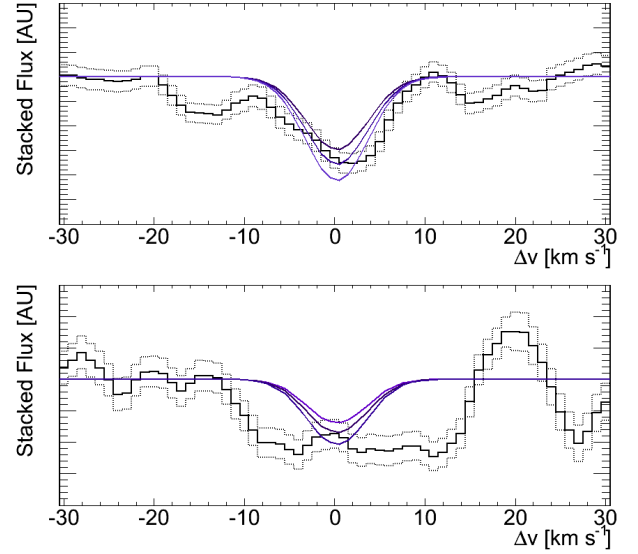


Fig. 3. Stacked spectra for HD $J = 0$ (seven lines, upper panel) and $J = 1$ (five lines, lower panel) transitions (solid), and the error (dotted). We also provide synthetic Voigt profile models with tied Doppler parameters and redshifts to those of H₂ $J = 0, 1$, for $\log N[\text{cm}^{-2}] = 13.3, 13.4, 13.5$, and $\log N[\text{cm}^{-2}] = 13.2, 13.3, 13.4$ respectively.

clearly see a line, while for $J = 1$ the obtained feature seems shapeless and is dominated by unsolved contaminations. The best column densities to match the obtained spectra are $N(\text{HD}, J = 0) \simeq 10^{13.4 \pm 0.1} \text{ cm}^{-2}$ and $N(\text{HD}, J = 1) \simeq 10^{13.3 \pm 0.1} \text{ cm}^{-2}$. These derived column densities should be considered as upper limits, i.e. $N(\text{HD}) \lesssim 10^{13.65 \pm 0.07} \text{ cm}^{-2}$. A higher S/N is needed to confirm the detection.

4.5. Neutral and singly-ionised carbon

Neutral carbon is detected in a single component at a redshift close to molecules, but 250 m s^{-1} blueshifted. Slight differences, of the order of less than 1 km s^{-1} in the position of H₂ and C I features have already been observed (see Srianand et al. 2012). In our case, this shift is observed over a large range of wavelengths and for several neutral carbon transitions, hence the effect is real. The absorption of C I and H₂ is expected to arise in the same gas because the two species are sensitive to the same radiation, but this is only true on the first order and self-shielding effects can be subtle so that the absorption profiles can still bear small differences in shape and distribution (see, e.g., Srianand & Petitjean 1998). Therefore, it is not so surprising to observe this small 250 m s^{-1} shift in the centroid of the two absorbing systems.

The column densities of the three sub-levels of the ground state are respectively, $N(\text{C I}) = 10^{12.56 \pm 0.07} \text{ cm}^{-2}$ for the $2s^2 2p^2 \ ^3P_0^e$ level, $N(\text{C I}^*) = 10^{12.41 \pm 0.14} \text{ cm}^{-2}$ for the $2s^2 2p^2 \ ^3P_1^e$ level, and $N_{\text{lim}}(\text{C I}^{**}) < 10^{11.95} \text{ cm}^{-2}$ for the $2s^2 2p^2 \ ^3P_2^e$ level. From the measured $N(\text{C I})$ and $N(\text{C I}^*)$ column densities, and for standard conditions, we would expect the C I** level to have $N(\text{C I}^{**}) \lesssim 10^{11.7} \text{ cm}^{-2}$ (see Noterdaeme et al. 2007b, Fig. 8), which is consistent with the observations.

We also detected ionised carbon in the excited state C II* ($2s^2 2p^2 \ ^3P_{3/2}^o$) in a single well-defined component, yielding $N(\text{C II}^*) = 10^{14.11 \pm 0.04} \text{ cm}^{-2}$, redshifted with respect to the neutral component by about 400 m s^{-1} . We also detected C II, however all components with $\Delta v \geq -30 \text{ km s}^{-1}$ are strongly saturated, hence no fit could be achieved.

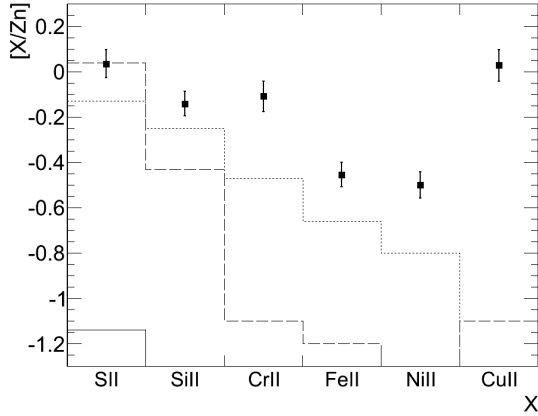


Fig. 4. Depletion factor, $[X/Zn]$, of different species relative to zinc calculated by integrating the column densities over the whole profile. Dotted, dashed, and solid lines correspond to depletion factors observed in, respectively, the halo, the warm, and cold ISM of the Galaxy (Welty et al. 1999). Note that the depletion factor observed in the Galaxy for copper is unavailable.

The results of the above fits are listed in Table 3, and the spectral features can be seen in Fig. A.9.

5. Physical characteristics of the absorption system at $z_{\text{abs}} \approx 2.6586$

5.1. Metallicity, depletion, and dust content

Integrating the column densities over all the components, we derive, $[Zn/H] = -0.91 \pm 0.09^4$ and $[S/H] = -0.87 \pm 0.09$. Again, the very good agreement between these two metallicity estimators shows that the estimated Zn II total column density is exact. A metallicity of $[X/H] \sim -0.9$ is slightly high for a $z \sim 2.5$ DLA (Prochaska et al. 2003), to be compared to a median metallicity of ~ -1.1 . This supports the idea that H₂ is expected to be found in relatively high-metallicity gas (Petitjean et al. 2006).

We now compare the relative abundances of elements to determine the depletion in this system. The relative amount of dust can be studied by the ratio of volatile versus refractory elements (e.g., Pettini et al. 1994). For this purpose, $[S/Fe]$ and $[Zn/Fe]$ are usually used (e.g., Vladilo 1998; Centurión et al. 2000), bearing in mind that sulphur is an α -element, hence its relative abundance may suffer some enhancement, and that whether zinc behaves as an α -element or an iron-peak element is not fully understood (see Rafelski et al. 2012). While Zn II transitions are weaker and blended with Mg I and Cr II, S II transitions fall in the Lyman- α forest and in a portion of the spectrum where the S/N is poor. We choose to present the analysis of depletion and dust content using Zn II, bearing in mind that the components on the blue side of the absorption profile should be taken as upper limits (see Sect. 4.2).

Depletion of iron and silicon relative to zinc is mild, $[Fe/Zn] = -0.45 \pm 0.06$ and $[Si/Zn] = -0.14 \pm 0.06$ when summing up all components, in good agreement with $[Fe/S]$ and $[Si/S]$ (see Table 2). The overall depletion pattern is shown in Fig. 4 and is consistent with what is seen in the galactic halo. Copper shows no depletion: $[Cu/H] = -0.88 \pm 0.10$, $[Cu/Zn] = -0.03 \pm 0.08$, and $[Cu/S] = -0.01 \pm 0.07$, similar to what was observed in the only other copper detection in a DLA system (Kulkarni et al. 2012), and in contrast to what is observed

⁴ By definition $[X/Y] \equiv \log[N(X)/N(Y)] - \log[N(X)/N(Y)]_{\odot}$ where all solar values are taken from Lodders (2003).

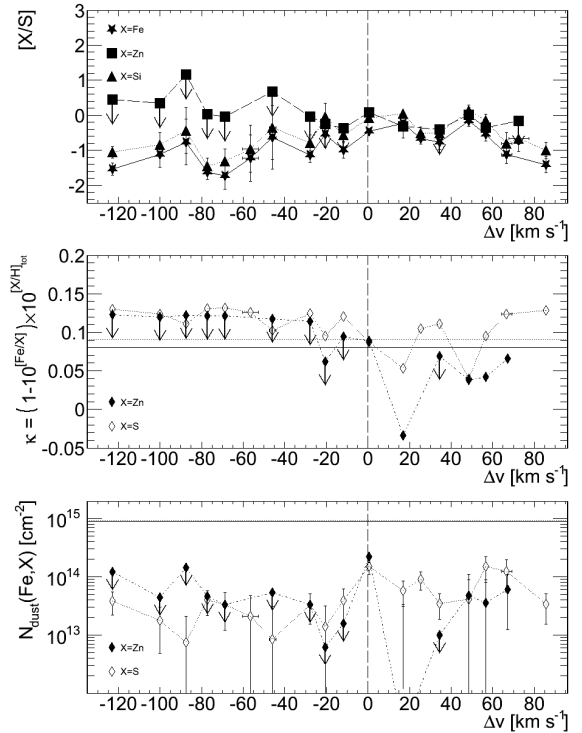


Fig. 5. Depletion and dust patterns through the absorption profile. *Top panel:* depletion of Fe, Zn, and Si with respect to S. *Middle panel:* dust to gas ratio computed with respect to Zn and S; the horizontal lines show the value of κ obtained when summing all components, using zinc (solid) and sulphur (dotted). *Bottom panel:* the iron column density in the dust phase computed with respect to Zn and S; horizontal lines mark the integrated value over all the profile, using zinc (solid) and sulphur (dotted). Vertical dashed lines show the C I and H₂ component at $z = 2.65859(7)$.

in the local ISM, with $[Cu/X] \sim -1.1$ in the warm ISM and $[Cu/X] \sim -1.4$ in the cold ISM (Cartledge et al. 2006). Note that the strictly solar relative abundances of copper, zinc, and sulphur indicates that we do not observe any α -element enrichment of zinc, contrary to what was suggested by Rafelski et al. (2012). This supports the usual interpretation that sub-solar $[Fe/Zn]$ ratios are rather the result of iron depletion into dust grains.

It has been argued that the depletion could be larger in the components where H₂ is found (see, e.g., Petitjean et al. 2002). We plot, in the top panel of Fig. 5, the depletion of S, Si, and Fe relative to Zn in each component versus the velocity position of the components with respect to the position of the C I and H₂ components located at $z = 2.65859(7)$. Notice that zinc and sulphur follow each other with mild differences on each edge of the absorption pattern. In particular, towards the blue, sulphur appears to be depleted with respect to zinc, which is unlikely to be a real effect, rather the result of the overestimation of Zn II column densities in those components. Hence, in the following component-by-component decomposition, we must critically compare the results using zinc or sulphur as references.

We have estimated the relative dust content on a single component, or a cloud, by means of the dust to gas ratio, $\kappa \approx (1 - 10^{[Fe/X]}) \times 10^{[X/H]}$, where $X = Zn$ or $X = S$ (see Prochaska et al. 2001 and Jenkins 2009). Averaging over the whole profile, we find $\kappa \approx 0.091$ when using sulphur and $\kappa \approx 0.080$ when using zinc, hence we estimate $\kappa \approx 0.08$. This is a typical value for high redshift DLAs (Srianand et al. 2005b). To compute κ component by component, we will assume that the metallicity is the same

Table 4. H₂ excitation temperatures in the $z_{\text{abs}} = 2.6586$ H₂-bearing cloud towards Q J 0643–5041 (all values in K).

T_{ij}	$i = 0$	$i = 3$
$j = 1$	$80.6^{+1.1}_{-1.0}$	97.9 ± 1.5
$j = 2$	$96.8^{+5.6}_{-5.0}$	$92.4^{+6.1}_{-7.1}$
$j = 3$	94.5 ± 1.2	...
$j = 4$	142 ± 1	560^{+93}_{-70}
$j = 5$	189 ± 3	569^{+67}_{-54}
$j = 6$	263 ± 7	907^{+186}_{-132}
$j = 7$	$80.6^{+1.0}_{-1.1}$	897^{+97}_{-80}

for all components and equal to the DLA mean metallicity. The result is shown in the middle panel of Fig. 5.

Finally, we can also estimate the Fe II equivalent column density trapped into dust grains in each component k : $N_{\text{dust}}^k(\text{Fe}, \text{X}) = (1 - 10^{[\text{Fe}/\text{X}]^k}) N^k(\text{X}) (N(\text{Fe})/N(\text{X}))^{\text{DLA}}$, where $(N(\text{Fe})/N(\text{X}))^{\text{DLA}}$ is the ratio of the total column densities in the DLA and $\text{X} = \text{Zn}$ or $\text{X} = \text{S}$ Vladilo et al. (see 2006). The values obtained at each component are shown in the bottom panel of Fig. 5. For reference, the total values are $N_{\text{dust}}^{\text{DLA}}(\text{Fe}, \text{Zn}) \simeq 10^{14.95} \text{ cm}^{-2}$ and $N_{\text{dust}}^{\text{DLA}}(\text{Fe}, \text{S}) \simeq 10^{14.97} \text{ cm}^{-2}$. This system is comparable to most H₂-bearing absorption systems at high redshift (Noterdaeme et al. 2008a). It is apparent from Fig. 5 that the depletion pattern is quite homogeneous through the profile, with only a mild indication for a higher dust column density at zero velocity. This indicates that the molecular component can easily be hidden in the metal profile. We note, however, that the Doppler parameter of the metal component that corresponds to H₂ is significantly lower than in the rest of the profile, indicating colder gas. In addition, the profile of highly ionised species such as C IV or Si IV (Fig. A.10) is comparatively weak at the position of H₂, revealing less ionisation in this component.

5.2. Thermal properties in the molecular cloud from H₂ rotational level populations

5.2.1. Excitation temperatures

The excitation temperature T_{ij} between two rotational levels $J = i, j$ is defined by

$$\frac{N_j}{N_i} = \frac{g_j}{g_i} \exp\left(-\frac{E_{ij}}{k_B T_{ij}}\right), \quad (1)$$

where g_J is the statistical weight of the J level and $E_{ij} \simeq (j(j+1) - i(i+1)) \times B$ is the energy difference between the rotational levels and B is the rotational constant of the H₂ molecule ($B/k_B = 85.3$ K). Using this relation, we compute the excitation temperatures T_{ij} with $i = 0, 3$ and $j = 1 \dots 7$. See the results in Table 4.

It is known that T_{01} is related to the temperature of formation on the surface of dust grains when the dominant thermalisation process is the formation of H₂, and to the kinetic temperature T_{kin} when the dominant thermalisation process is collisions. In thick, self-shielded molecular clouds where $N(\text{H}_2) \geq 10^{16.5} \text{ cm}^{-2}$, T_{01} is a good tracer of the kinetic temperature (see Srianand et al. 2005a; Roy et al. 2006, and references therein). Here, $T_{\text{kin}} \simeq T_{01} = (80.6^{+1.1}_{-1.0})$ K, as in most high-redshift H₂-bearing clouds detected so far. Such a temperature is also very close to that of the ISM of the MW or the Magellanic Clouds, where the average temperature is found to

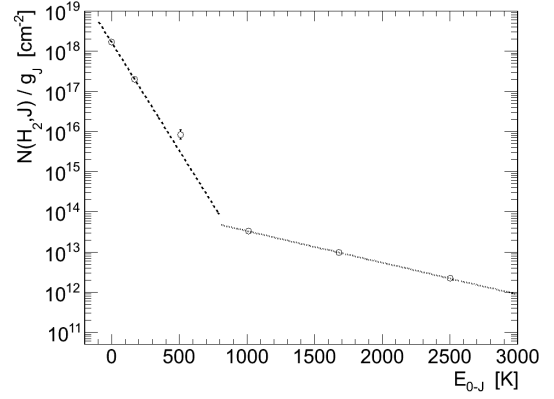


Fig. 6. Excitation diagram of H₂. Two different behaviours are characterised by two different excitation temperatures, one for $J = 0, 1$, and 2 and one for $J = 3, 4$, and 5. The following two levels are somehow incompatible with both of these characteristic temperatures, however, the uncertainty on their column densities is too large to elaborate further.

be (77 ± 17) K (Savage et al. 1977) and (82 ± 21) K (Tumlinson et al. 2002), respectively, suggesting a cold neutral medium.

5.2.2. Ortho-para ratio and local thermal equilibrium

The ortho-para ratio (OPR), i.e., the ratio of the total population (column densities) of ortho (even J) levels to that of para (odd J) levels, is another tracer of the state of the gas in the molecular gas, and is given by

$$OPR = \frac{\sum_{J=\text{odd}} N(J)}{\sum_{J=\text{even}} N(J)}. \quad (2)$$

Here we measure $OPR = 1.06$. If we assume the H₂-bearing gas is at local thermal equilibrium (LTE), then we can relate the OPR to the equilibrium distribution with a single temperature for the whole gas and estimate T^{LTE} :

$$OPR_{\text{LTE}} \simeq 3 \frac{\sum_{J=\text{odd}} (2J+1) \exp\left(-\frac{BJ(J+1)}{k_B T^{\text{LTE}}}\right)}{\sum_{J=\text{even}} (2J+1) \exp\left(-\frac{BJ(J+1)}{k_B T^{\text{LTE}}}\right)}, \quad (3)$$

where k_B is the Boltzmann constant. When the kinetic temperature is high, the OPR is expected to reach a value of 3, while in cold neutral media its value is expected to be below 1 (Srianand et al. 2005a). Hence, the OPR, in agreement with the excitation temperature T_{01} , also points towards a cold neutral medium.

5.2.3. Excitation diagram

The excitation diagram, i.e., the ratio of the column density in a level to its statistical weight versus the energy difference between this level and $J = 0$, is presented in Fig. 6. As is shown by the two fitting lines, there seems to be two different excitation regimes, namely one for levels $J = 0 \dots 2$ with $T_{0J} = (80.7 \pm 0.8)$ K, and another for levels $J = 3 \dots 5$ with $T_{3J} = (551^{+42}_{-37})$ K. We limit the analysis to $J = 5$ since the uncertainty on the column densities of $J = 6$ and $J = 7$ is large. We can readily see that $T_{0J, J=1,2}$ is compatible with T_{01} . If $T_{ij} \simeq T(OPR) (\simeq T_{01})$, then the excitation is dominated by collisions (Srianand et al. 2005a), and this seems to be the case below $J = 3$. From this level and above, other mechanisms intervene, such as radiation pumping (excitation of lower levels to higher

levels by UV radiation) or formation pumping (preferred formation of H₂ in excited states, which then de-excite to the lower levels). From Table 4 we see that T_{3J} is of the same order as T_{34} and T_{35} .

The Doppler parameter increases with increasing rotational level. This could be the result of higher rotational levels arising mostly from the outer parts of the cloud, which are heated by photoelectric effect on dust grains by the surrounding UV flux (Ledoux et al. 2003).

5.3. Ambient UV flux

5.3.1. The UV flux from heating/cooling equilibrium

We proceed to estimate the ambient UV flux using the same procedure used by Wolfe et al. (2003). Assuming equilibrium between the photo-electric heating of the gas and the cooling by the C II* ($^2P_{3/2} \rightarrow ^2P_{1/2}$) emission, together with similar interstellar medium conditions between the galaxy and DLAs (same type of dust grains, temperature, and density Weingartner & Draine 2001), we can write $\frac{l_c}{k_{MW}} \approx \kappa \frac{F_{UV}}{F_{MW}}$, where $\kappa = k_{DLA}/k_{MW}$ is the relative dust to gas ratio, and k_{DLA} and k_{MW} are the local dust to gas ratio at the DLA and the MW and l_c the cooling rate.

In the DLA we studied, we estimated the relative dust to gas ratio to be $\kappa \approx 0.08$. Then, the average energy loss per hydrogen atom determines the cooling rate

$$l_c = \frac{h\nu(^2P_{3/2} \rightarrow ^2P_{1/2}) N(C II^* ^2P_{3/2}) A_{21}}{N(H)} \text{erg s}^{-1}, \quad (4)$$

with $\lambda(^2P_{3/2} \rightarrow ^2P_{1/2}) \approx 158 \mu\text{m}$ and $A_{21} \approx 2.4 \times 10^{-6} \text{s}^{-1}$, the wavelength and decay rate of the spontaneous photon emitting $^2P_{3/2} \rightarrow ^2P_{1/2}$ transition respectively (Pottasch et al. 1979; Wolfe et al. 2003). We estimate $N(C II^*) \approx 10^{14.1} \text{cm}^{-2}$ (see Table 3) and $N(H I) \approx 10^{21.0} \text{cm}^{-2}$. This leads to $l_c \approx 10^{-26.4} \text{erg s}^{-1}$ per hydrogen atom. From this we derive $F_{UV} \sim 0.82 \times F_{UV}^{MW}$.

5.3.2. Rotational excitation and radiation field

We estimate the ambient UV radiation, using the excitation of the high J levels, since we have seen that for $J \geq 3$, the excitation temperature as deduced from the level populations is substantially larger than T_{kin} . Hence, these levels are excited by fluorescence, but also, the formation of H₂ in high rotational levels. Following Noterdaeme et al. (2007b), formation pumping is related, at equilibrium, to the photodissociation rate such that $R_{form} n_p n(H) = R_{diss} n(H_2)$, where R_{form} , n_p and R_{diss} stand for the H₂ formation rate, the proton density, and the H₂ photodissociation rate. The latter is related to the photoabsorption rate β , which brings us to the ambient UV flux, by $R_{diss} = \zeta \beta$, where $\zeta = 0.11$ is the fraction of photodissociation to photoabsorption. This yields $R_{form} n_p n(H)/n(H_2) = R_{diss} = \zeta \beta$. Hence, we write the equilibrium between spontaneous decay of $J = 4, 5$ levels (with transition probabilities $A_{4 \rightarrow 2} = 2.8 \times 10^{-9} \text{s}^{-1}$ and $A_{5 \rightarrow 3} = 9.9 \times 10^{-9} \text{s}^{-1}$), and UV pumping from the most populated lower levels $J = 0, 1$ (with efficiencies $p_{4,0} = 0.26$ and $p_{5,1} = 0.12$ and absorption rates β_0 and β_1) and formation pumping into $J = 4, 5$ levels (with $f_4 \approx 0.19$ and $f_5 \approx 0.44$ fractions) as

$$p_{4,0} \beta_0 n(H_2, J=0) + f_4 R_{form} n_p n(H) = A_{4 \rightarrow 2} n(H_2, J=4) \quad (5)$$

and

$$p_{5,1} \beta_1 n(H_2, J=1) + f_5 R_{form} n_p n(H) = A_{5 \rightarrow 3} n(H_2, J=5). \quad (6)$$

Dividing by the H₂ density, assuming the homogeneity of the gas cloud (and therefore $n(H_2, J)/n(H_2) = N(H_2, J)/N(H_2)$) and rearranging these equations we get

$$\beta_0 \left(p_{4,0} \frac{N(H_2, J=0)}{N(H_2)} + \zeta f_4 \right) = A_{4 \rightarrow 2} \frac{N(H_2, J=4)}{N(H_2)} \quad (7)$$

and

$$\beta_1 \left(p_{5,1} \frac{N(H_2, J=1)}{N(H_2)} + \zeta f_5 \right) = A_{5 \rightarrow 3} \frac{N(H_2, J=5)}{N(H_2)}. \quad (8)$$

Using these relations we get $\beta_0 \approx (4.9 \pm 0.2) \times 10^{-13} \text{s}^{-1}$ and $\beta_1 \approx (18.8 \pm 1.9) \times 10^{-13} \text{s}^{-1}$. These are extremely low values that can be explained by the shielding of the inner part of the cloud by outer layers. The large $\log N(H_2)/N(C I) = 5.97 \pm 0.09$ ratio measured in the cloud confirms, as it has already been pointed out, that large H₂ column densities at high redshift, and in particular large $\log N(H_2)/N(C I)$, are associated with low photoabsorption rates (see Noterdaeme et al. 2007b, Fig. 7).

The total shielding S is the product of the molecular hydrogen self-shielding, estimated by $S_{H_2} \approx (N(H_2)/10^{14} \text{cm}^{-2})^{-0.75}$ by the dust extinction $S_{dust} = \exp(-\tau_{UV})$, and allows us to relate the photodissociation rate to J_{LW} , the UV intensity at $h\nu = 12.87 \text{eV}$ averaged over the solid angle, with the relation $R_{diss} = \zeta \beta = 4\pi 1.1 \times 10^8 J_{LW} S$. The dust optical depth can be approximated by $\tau_{UV} \approx 0.879 \kappa (N(H)/10^{21} \text{cm}^{-2})$ (see Noterdaeme et al. 2007a), where κ is the dust to gas ratio, as discussed in Sect. 5.1. Hence, $\tau_{UV} \approx 0.07$ leads to $S \approx (4 \times 10^{-4}) \times (0.9) \approx 3.8 \times 10^{-4}$. Self-shielding is the dominant shielding mechanism as usual. Given this and adopting $\beta = \beta_0$ we arrive at $J_{LW} \approx 8 \times 10^{-11} \beta_0/S \approx 8.5 \times 10^{-20} \text{erg s}^{-1} \text{cm}^{-2} \text{Hz}^{-1} \text{sr}^{-1}$, which is a factor $\chi = 2.6$ larger than in the solar vicinity. Note that this is larger by about a factor of four compared to the value derived from the C II* absorption line. The two measurements are comparable, however, and have no a priori reason to match exactly as the C II* measurement corresponds to a mean flux in the host galaxy when the H₂ measurement is related to the flux in the vicinity of the H₂-bearing cloud.

Following Hirashita & Ferrara (2005), we can relate χ to the surface star forming rate $\Sigma_{SFR} \approx \chi \times 1.7 \times 10^{-3} M_{\odot} \text{yr}^{-1} \text{kpc}^{-2} \approx 4.4 \times 10^{-3} M_{\odot} \text{yr}^{-1} \text{kpc}^{-2}$.

5.4. Neutral carbon fine structure and the extension of the molecular cloud

The relative populations of the fine-structure levels of neutral carbon ground state is determined by the ambient conditions through collisions and excitation by the UV flux and the CMB radiation. We can estimate the density of the gas because for densities $\geq 10 \text{cm}^{-3}$ and temperatures $T_{kin} \sim 100 \text{K}$, these populations depend primarily on the hydrogen density (see Silva & Viegas 2002, Fig. 2).

We measure $N(C I^*)/N(C I) = 10^{-0.10 \pm 0.11}$ and estimate the hydrogen density to be in the range $n(H) \approx (40-140) \text{cm}^{-3}$ with a central value of 80cm^{-3} (from Noterdaeme et al. 2007b, Fig. 8).

We thus estimate the characteristic length of the cloud to be $l \approx N(H I)/n(H)$: $2.3 \text{pc} \leq l \leq 7.9 \text{pc}$. The H I column density in the main component, which bears molecules, is certainly overestimated, since species such as Fe II, Si II, O I, C II, or Ni II are found in many components spanning over 200km s^{-1} . Therefore, we can safely conclude that $l < 8 \text{pc}$. For simplicity, we assume a spherical shape, which translates into an angular size of $\theta_{DLA} < 0.9 \text{mas}$. However, there is no reason

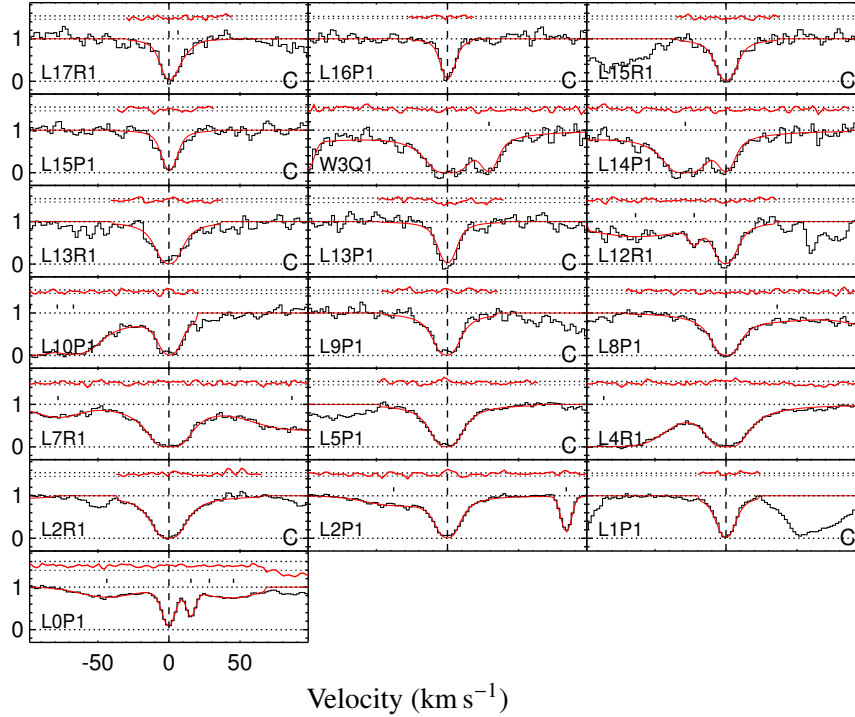


Fig. 7. Absorption profile of H_2 transitions from the $J = 1$ level and the best-fitting Voigt profile. The normalised residual (i.e., $([data]-[model])/[error]$) for each fit is also shown in the top of each panel along with the 1σ line. We present the clean absorption lines by putting a letter “C” in the right bottom of these transitions.

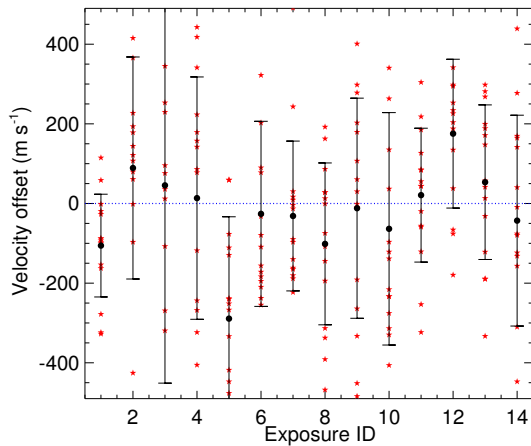


Fig. 8. Results of cross-correlation analysis between individual spectra and the combined one for each order. Bars present the standard deviations of the shifts measured for individual spectra.

for the length scale along the line-of-sight to be the same as the transverse extension. Moreover, the average density within the molecular cloud could be slightly different, since there is a small 250 m s^{-1} displacement in the centroid of the neutral carbon and H_2 absorption features.

Bearing this in mind, for comparison, the angular size of a typical BLR (of extension $l_{\text{BLR}} \sim 1 \text{ pc}$) amounts to $\theta_{\text{BLR}} \sim 0.1 \text{ mas}$. This is fully consistent with full coverage of the BLR by the DLA. Nonetheless, the size of the molecular cloud could be much smaller. Balashev et al. (2011) estimated that the molecular cloud at $z = 2.34$ towards Q1232+082 has an extension of $(0.15 \pm 0.05) \text{ pc}$, hence it could well be two orders of magnitude smaller than 0.9 mas . Given this, it is impossible to conclude the

actuality of the partial coverage of the BLR by the H_2 -bearing cloud.

6. Constraints to the cosmic variation of the proton-to-electron mass ratio with Q J 0643–5041

In the case of H_2 molecule, the energy difference between rotational states and vibrational states is proportional to the reduced mass of the system and its square root, respectively. Using intervening molecular absorption lines seen in the high- z quasar spectra for measuring $\Delta\mu/\mu$ (i.e., $\Delta\mu/\mu \equiv (\mu_z - \mu_0)/\mu_0$ where μ_z and μ_0 are the values of proton-to-electron mass ratio at redshift z and today) in the distant universe was first proposed by Thompson (1975).

The sensitivity of the wavelength of the i 'th H_2 transition to the variation of μ is generally parametrised as

$$\lambda_i = \lambda_i^0 (1 + z_{\text{abs}}) \left(1 + K_i \frac{\Delta\mu}{\mu} \right), \quad (9)$$

where λ_i^0 is the rest frame wavelength of the transition, λ_i is the observed wavelength, K_i is the sensitivity coefficient of i 'th transition, given by $K_i = d \ln \lambda_i^0 / d \ln \mu$, and z_{abs} is the redshift of the H_2 system. Here we use the most recent data on K_i given by Meshkov et al. (2006), Ubachs et al. (2007) and the rest wavelengths and oscillator strengths from Malec et al. (2010). Equation (9) can be rearranged as

$$z_i = z_{\text{abs}} + CK_i, \quad C = (1 + z_{\text{abs}}) \frac{\Delta\mu}{\mu}, \quad (10)$$

which clearly shows that z_{abs} is only the mean redshift of transitions with $K_i = 0$. The redshift of the i 'th H_2 transition is denoted

Table 5. $\Delta\mu/\mu$ estimations using H₂ lines in the $z_{\text{abs}} = 2.6586$ H₂-bearing cloud towards Q J 0643–5041.

$\Delta\mu/\mu \times 10^6$								
1 component					shift-corrected			
Fit	Error	b	$\Delta\mu/\mu$	χ^2_{red}	AICC	$\Delta\mu/\mu$	χ^2_{red}	AICC
l-b-l	bootstrap	tied	5.0 ± 6.1	1.57	...	8.1 ± 6.6	1.53	...
l-b-l	bootstrap	free	4.6 ± 5.9	1.55	...	7.6 ± 6.4	1.51	...
VPFIT	weighted	tied	4.8 ± 4.2	1.58	7318	5.9 ± 4.2	1.57	7299
VPFIT	weighted	free	5.5 ± 4.3	1.58	7301	6.7 ± 4.2	1.55	7204
2 components					shift-corrected			
VPFIT	weighted	free	6.5 ± 4.3	1.57	7253	7.4 ± 4.3	1.53	7150

Notes. The quoted errors in $\Delta\mu/\mu$ come mainly from statistical errors.

by z_i . The expression in Eq. (10) is sometimes presented as

$$z_{\text{red}} \equiv \frac{(z_i - z_{\text{abs}})}{(1 + z_{\text{abs}})} = K_i \frac{\Delta\mu}{\mu}, \quad (11)$$

which shows the value of $\Delta\mu/\mu$ can be determined, using the reduced redshift (z_{red}) versus K_i . At present, measurements of $\Delta\mu/\mu$, using H₂ at $z \geq 2$, are limited to six H₂-bearing DLAs (see Varshalovich & Levshakov 1993; Cowie & Songaila 1995; Levshakov et al. 2002; Ivanchik et al. 2005; Reinhold et al. 2006; Ubachs et al. 2007; Thompson et al. 2009; Wendt & Molaro 2011, 2012; Rahmani et al. 2013). All these measurements are consistent with $\Delta\mu/\mu$ being zero at the level of 10 ppm. Here we present a new $\Delta\mu/\mu$ constraint, using the $z_{\text{abs}} = 2.6586$ absorbing system towards Q J 0643–5041.

Like in Rahmani et al. (2013) we use two approaches to measure $\Delta\mu/\mu$. In the first approach, we fit the H₂ lines, using a single velocity component, and estimate the redshift for each H₂ transitions, and measure $\Delta\mu/\mu$ using Eq. (11). In the second approach, we explicitly use $\Delta\mu/\mu$ as one of the fitting parameters in addition to N , b , and z in VPFIT. This approach allows for a multi-component fit of the H₂ lines. The results of $\Delta\mu/\mu$ for various approaches are given in Table 5.

To carry out a measurement of μ , we need to choose a suitable set of H₂ lines. Although H₂ absorption from high J -levels ($J = 4-7$) is detected towards Q J 0643–5041, it is too weak to lead to very accurate redshift measurements, as required for this study. Therefore, we reject H₂ lines from these high- J levels while measuring $\Delta\mu/\mu$, and only use H₂ absorption features from $J = 0-3$. By carefully inspecting the combined spectrum, we identified 81 lines suitable for $\Delta\mu/\mu$ measurements. A list of H₂ transitions we used is tabulated in Table B.1, where clean lines are highlighted. Thirty-eight out of 81 lines are mildly blended with the intervening Lyman- α absorption of the intergalactic medium. We accurately model surrounding contaminations using multi-component Voigt-profile fitting, while simultaneously fitting the H₂ lines (see Fig. 7).

6.1. Systematic wavelength shifts: cross-correlation analysis

D’Odorico et al. (2000) have shown that the resetting of the grating between an object exposure and the ThAr calibration lamp exposure can result in an error of the order of a few hundred meters per second in the wavelength calibration. To minimise the errors introduced via such systematics in our $\Delta\mu/\mu$ measurements, we do not use those exposures without attached mode ThAr calibration lamps. We further exclude the exposure with 1389 s of EXPTIME (10th row of Table 1) as the quality of this spectrum is very poor. Therefore, the combined spectrum to be used

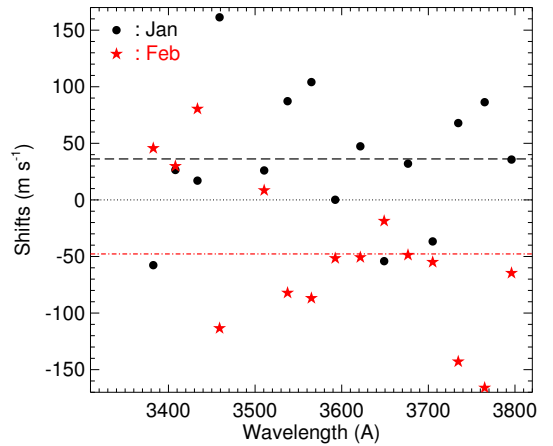


Fig. 9. Cross-correlation analysis between the combined spectrum of the exposures taken in early January and combined spectrum of those in February.

for measuring $\Delta\mu/\mu$ is made of 14 exposures with S/N of between 11–31 over our wavelength range of interest.

The shortcomings of the ThAr calibration of VLT/UVES spectra have been shown by a number of authors (Chand et al. 2006; Levshakov et al. 2006; Molaro et al. 2008; Thompson et al. 2009; Whitmore et al. 2010; Agafonova et al. 2011; Wendt & Molaro 2011; Rahmani et al. 2012, 2013; Agafonova et al. 2013). Here we carry out a cross-correlation analysis between the combined spectrum and the individual exposures to estimate the offset between them over the wavelength range of echelle orders of the blue arm. To do so we rebin each pixel of size 2.0 km s^{-1} into 20 sub-pixels of size 100 m s^{-1} and measure the offset as corresponding to the minimum value of the χ^2 estimator of the flux differences in each window (see Rahmani et al. 2013, for more detail). Each cross-correlating window spans an echelle order. The accuracy of this method is well demonstrated via a Monte Carlo simulation analysis in Rahmani et al. (2013). Figure 8 shows the results of such cross-correlation analysis.

We observe that EXP5 has the maximum constant offset of -287 m s^{-1} , while other exposures show constant offsets consistent with zero shift. We correct the measured shifts for individual orders of each exposure and make a new combined spectrum, and subsequently analyse its impact on $\Delta\mu/\mu$.

To check the stability of the spectra over a one-month period of observations, we make two combined spectra of EXP7 – EXP14 and EXP17 – EXP20. Fig. 9 shows the results of cross-correlation of these two spectra with the combined spectrum. The first three circle-asterisks pairs at $\lambda < 3450 \text{ \AA}$ and the pair at 3650 \AA present an opposite trend in comparison to the rest

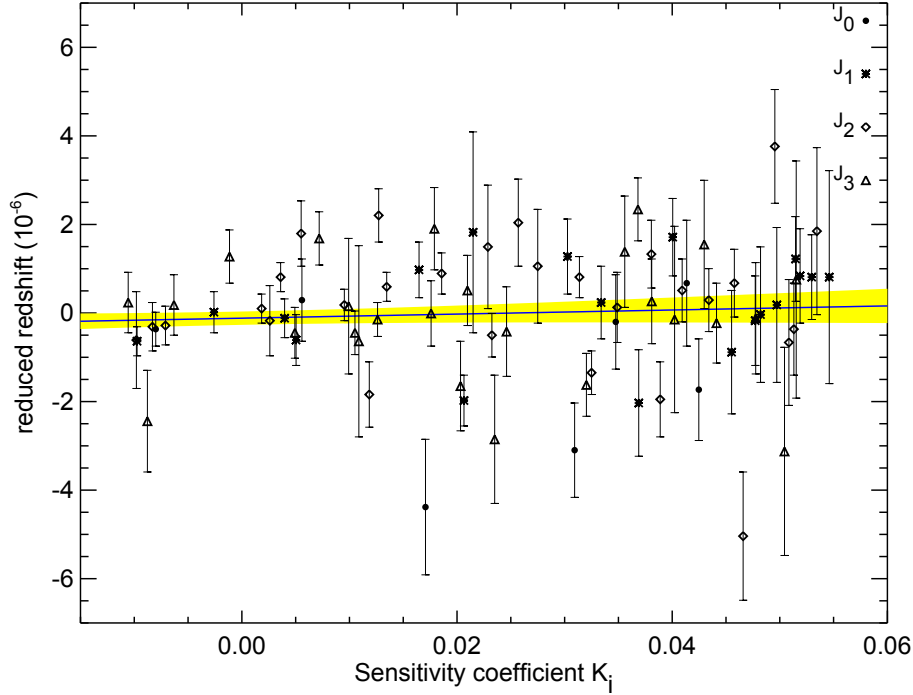


Fig. 10. Reduced redshift vs. the K_i for the fit with different b for different J -levels. Different J -levels are plotted with different symbols. The best-fitting linear line is also shown. The yellow region shows the 1σ error in the fitted line.

of the pairs. However, apart from a constant shift of $\sim 80 \text{ m s}^{-1}$, there is not any strong evidence for the existence of possible wavelength dependent systematic errors.

Furthermore, Rahmani et al. (2013) compared the asteroid spectra from UVES and the solar spectrum to discover a wavelength dependent systematic error in UVES observations. Moreover, they showed that such systematic errors can mimic a $\Delta\mu/\mu$ in the range of 2.5–13.7 ppm, which changes in different epochs from 2010 to 2012. Such a systematic error cannot be revealed from the cross-correlation analysis between the individual exposures and the combined spectrum of this quasar, i.e., without a reference spectrum. Unfortunately, we do not have asteroid observations with the same settings of and close in time to our science observations, hence we are not in a position to check whether such a drift is present in our data. Ceres has been observed with the 346 setting of UVES on 05-12-2007 and without attached mode ThAr lamp. However, such an observation is not an appropriate reference to study the effect of a wavelength drift in 390 setting observations, hence we have not corrected the data using this drift measurement.

6.2. Limits on $\Delta\mu/\mu$ at $z = 2.6586$: first approach

Most measurements of $\Delta\mu/\mu$ using H_2 use the measured slope between the reduced redshifts and K_i . The most important step in this approach is to measure the redshifts and the associated errors of a set of chosen H_2 absorption lines.

To measure the redshifts of the suitable H_2 lines, first we choose a model in which all the J -levels have the same b parameter. The best-fitting model in this case has a reduced χ^2 (χ_{red}^2) of 1.57. Inspecting the spectrum and the normalised residual ($([\text{data}] - [\text{model}]) / [\text{error}]$) of the best-fitting model show that the relatively large χ_{red}^2 is mainly due to the underestimation of the flux error and not due to a poor Voigt profile model. A z -vs.- K analysis of the fitted redshifts based on a linear regression yields $\Delta\mu/\mu = (5.0 \pm 6.1) \text{ ppm}$. The quoted error is obtained using

the bootstrap technique. Indeed, we generate 2000 random realizations of the measured redshifts and estimate $\Delta\mu/\mu$ for each realization. We finally quote the 1σ scatter of the 2000 $\Delta\mu/\mu$ thus obtained as the estimated error.

The physical conditions in this H_2 system and also other H_2 systems (see Noterdaeme et al. 2007a) shows that different J -levels may bear different turbulent broadening parameters. In particular, $J = 0$ and 1 have smaller b -parameters compared to higher J -levels. Hence we define a second model in which different J -levels are allowed to have different b -parameters. The best such fitted model has a $\chi_{\text{red}}^2 = 1.55$. The z -vs.- K analysis out of these fitted redshifts yields $\Delta\mu/\mu = (4.6 \pm 5.9) \text{ ppm}$, which is very much consistent with the value obtained with the first model. Figure 10 presents the results of this fit.

Applying the above discussed models on the shift-corrected combined spectrum, we find $\Delta\mu/\mu$ of $(8.1 \pm 6.6) \text{ ppm}$ and $(7.6 \pm 6.4) \text{ ppm}$ for tied and untied b , respectively. While consistent, both values are $\sim 3 \text{ ppm}$ larger in comparison with the uncorrected values.

6.3. Limits on $\Delta\mu/\mu$ at $z = 2.6586$ directly from VPFIT

Next, we include $\Delta\mu/\mu$ as a parameter of the fits. Using a single component model and assuming the fitted b parameter value to be the same for all J -levels, the best fit converges to $\Delta\mu/\mu = (4.8 \pm 4.2) \text{ ppm}$ with an overall reduced χ^2 of 1.60. The quoted error of 4.2 ppm in $\Delta\mu/\mu$ is already scaled with $\sqrt{\chi_{\text{red}}^2}$. We implement similar scaling of the statistical errors each time we find $\chi_{\text{red}}^2 > 1.0$. This result is very much consistent with the previous findings. We apply the same analysis to the combined spectrum made of CPL generated 1-d spectra. For this model, we find $\Delta\mu/\mu = (9.1 \pm 4.7) \text{ ppm}$ for such a combined spectrum. The two values differ by $\sim 1\sigma$. Therefore, systematic errors as large as 4.3 ppm can be produced if we use the final 1-d spectra generated by CPL.

In the last column of Table 5, we provide the Akaike information criteria (AIC; Akaike 1974) corrected for the finite sample size (AICC; Sugiura 1978) as given in Eq. (4) of King et al. (2011). While the $\Delta\mu/\mu$ error from the bootstrap is sensitive to the redshift distribution of H₂ lines, the VPFIT errors purely reflect the statistical errors. Hence, the larger error from the bootstrap method can be used to quantify the associated systematic errors. If we quadratically add 4.4 ppm to the VPFIT error, which is 4.2 ppm, we get the bootstrap error. Therefore, we can associate a systematic error to each VPFIT measurement by comparing the VPFIT error with the bootstrap error.

In the fourth line of Table 5, we present the results of the fit when b parameters in different J -levels are allowed to be different. While the best-fitting $\Delta\mu/\mu$ of (5.5 ± 4.3) ppm is consistent with the case when we use a common b value for all J -levels, the AICC value is slightly better. In this case, the comparison of the estimated error from the bootstrap method (second line in Table 5) suggests a systematic error of 4.0 ppm.

We also consider two velocity component models. The two-component fit with common b for different J levels systematically drops one of the components while minimizing the χ^2 . However, when the Doppler parameter is different for different J -levels we are able to obtain a consistent two-component fit. The two components are separated by (0.19 ± 0.11) km s⁻¹. We find $\Delta\mu/\mu = (6.5 \pm 4.3)$ ppm for such a fit. The results are summarised in the last row of Table 5. We also present the two-component fit results using shift-corrected data in Table 5. The values of $\Delta\mu/\mu$ are larger by ~ 2 – 3 ppm for all of the models after correcting the spectra for the shifts. It is clear that while there is a marginal improvement in the χ^2_{red} and AICC the final results are very much consistent with one another. Moreover, we see that the best model is the two-component model for both shift-corrected and not corrected spectra, based on the data in Table 5. Therefore, we choose the two-component H₂ fit as the best model of the data. As in Rahmani et al. (2013) we quote the final error in $\Delta\mu/\mu$ including the systematic error obtained above and the statistical error given by VPFIT. Therefore, we consider the best-fitting measurement to be $\Delta\mu/\mu = (7.4 \pm 4.3_{\text{stat}} \pm 5.1_{\text{sys}})$ ppm.

7. Conclusions and discussion

We have studied the physical properties of the molecular hydrogen gas associated with the DLA system at $z_{\text{abs}} = 2.6586$ towards the high redshift ($z_{\text{em}} = 3.09$) quasar Q J0643–5041, using VLT-UVES data with a total integration time of 23 h.

We find that the DLA ($\log N(\text{H I})(\text{cm}^{-2}) = 21.03 \pm 0.08$) has typical characteristics of the high-redshift DLA population associated with molecular clouds, with metallicity $[\text{Zn}/\text{H}] = -0.91 \pm 0.09$ and depletion of iron relative to zinc $[\text{Zn}/\text{Fe}] = 0.45 \pm 0.06$, and a hydrogen molecular fraction of $\log f = -2.19^{+0.07}_{-0.08}$. Molecular hydrogen is detected up to $J = 7$ and the excitation diagram exhibits two temperatures, $T = 80.7 \pm 0.8$ and 551 ± 40 K for $J < 3$ and > 3 , respectively. The ambient UV radiation field, derived from the C II $\lambda 156\mu$ radiation, and from the analysis of the H₂ UV pumping, is of the order of the MW field.

We study the possibility that the H₂ bearing cloud does not cover the background source completely. For this, we analyse the distribution of residual flux observed at the bottom of saturated H₂ lines and estimate the relative contributions from the BLR and AGN continuum to the emitted flux. We find that there is weak evidence for a possible excess of residual light from the BLR. Given the density derived from the C I absorption lines (n_{H} in the range 40 – 140 cm⁻³) and the H I column density, we derive a dimension of the cloud of the order of 2.5 – 8 pc. This is

consistent with the fact that the residual flux, if real, is small and the cloud covers most of the BLR.

We have attempted to measure HD at the same redshift as H₂. By stacking the best defined features, we have been able to set an upper limit of $N(\text{HD}) \lesssim 10^{13.65 \pm 0.07} \text{cm}^{-2}$. Deuterium is formed in the primordial universe and is subsequently progressively destroyed in stars. Therefore, one expects the abundance of deuterium to be at most equal to the primordial value, stemming from primordial nucleosynthesis, in most metal poor gas, and smaller if its local destruction is already onset. In molecular clouds, deuterated molecular hydrogen is expected to form along with H₂ in shielded environments. In high redshift quasar absorption lines, only six detections have been reported so far: towards Q1232+082 (Varshalovich et al. 2001; Ivanchik et al. 2010); towards Q143912.04+111740.4 (Srianand et al. 2008; Noterdaeme et al. 2008b); towards J0812+3208 and Q1331+170 (Balashev et al. 2010); towards J123714.60+064759.5 (Noterdaeme et al. 2010); and towards J21230500 (Tumlinson et al. 2010). When HD is detected, it is possible to probe the deuterium abundance by studying the $N(\text{HD})/2N(\text{H}_2)$ ratio, which should be a lower limit for D/H. A smaller deuterium fraction in molecules would be the consequence of differences in chemical molecular formation processes and of differential photo-dissociation (see, e.g., Tumlinson et al. 2010). All observations up to now seem to show that the measured HD/2H₂ ratio is surprisingly high (Balashev et al. 2010; Ivanchik et al. 2010), with typical values of f_{D} between -4.8 and -4.4 (Tumlinson et al. 2010). The D fraction, $f_{\text{D}} \approx N(\text{HD})/2N(\text{H}_2)$, in this system is then $\lesssim (6.50 \pm 1.07) \times 10^{-6} = 10^{-5.19 \pm 0.07}$, to be compared to the primordial abundance of deuterium, which is of $\log D/H = -4.60$. Hence, in the cloud at $z_{\text{abs}} = 2.6586$ towards Q J0643–5041, the relative deuterium abundance is half an order of magnitude lower than the primordial value. This value can also be compared to what is seen in the Milky Way. Lacour et al. (2005) find that f_{D} increases with increasing molecular fraction. Extrapolating towards the molecular fraction of $f = -2.19$ would yield $f_{\text{D}} \approx -7.5$, which is two orders of magnitude below the upper limit we determine. Large HD/2H₂ ratios seem to be common at high redshift and remain unexplained (see Tumlinson et al. 2010).

We take fourteen ~ 1 h exposures with attached ThAr calibrations to reduce systematics in the wavelength calibration. We used this data to constrain the variation of the μ at the redshift of the DLA. We selected 81 H₂ lines suitable for $\Delta\mu/\mu$ measurements. We find that the two-velocity component model with untied Doppler parameters between different rotational levels can best model the absorption profiles of H₂ lines of this system. We measure $\Delta\mu/\mu = (7.4 \pm 4.3_{\text{stat}} \pm 5.1_{\text{sys}})$ ppm for such a model. Our result is consistent with no variation of μ over the last 11.2 Gyr. If we add the systematic and statistical errors quadratically, we get the total error of 6.7 ppm in our $\Delta\mu/\mu$ measurement. This is $\sim 30\%$ smaller than the error (10.1 ppm) in $\Delta\mu/\mu$, which we have obtained in a recent study of an H₂ system towards HE 0027–1836 at $z_{\text{abs}} = 2.4018$ (Rahmani et al. 2013). The main reason for the smaller error in the current study is the wider K_i range covered by the H₂ lines towards Q J0643–5041 compared to those of HE 0027–1836. This is an important consideration that should be taken into account in selection of systems for the study of $\Delta\mu/\mu$.

Figure 11 summarises $\Delta\mu/\mu$ measurements based on different approaches at different redshifts. Our new measurement is consistent with all the other measurements based on H₂ lines. However, we also note that like the majority of other studies, our $\Delta\mu/\mu$ is positive although consistent with zero.

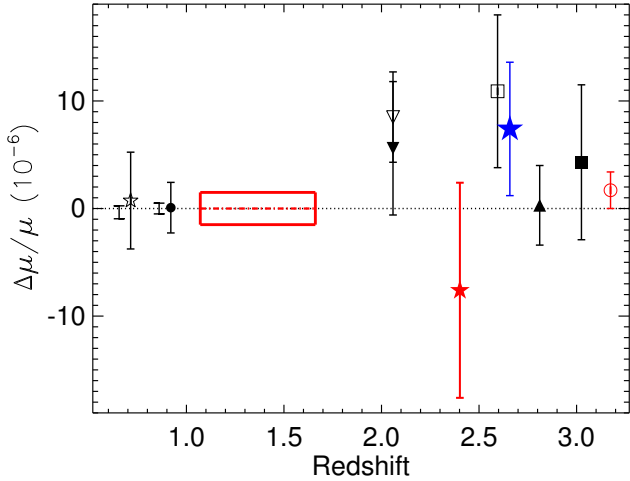


Fig. 11. Comparison of $\Delta\mu/\mu$ measurement in this work and those in the literature. All measurements at $2.0 < z < 3.1$ are based on the analysis of H_2 absorption. The filled larger blue star shows our result and the smaller red star shows the result from [Rahmani et al. \(2013\)](#). The downwards empty and filled triangles are the $\Delta\mu/\mu$ measurements from [van Weerdenburg et al. \(2011\)](#) and [Malec et al. \(2010\)](#). The filled upward triangle and the empty and filled squares are, respectively, from [King et al. \(2008; 2011\)](#), and [Wendt & Molaro \(2012\)](#). The solid box and the open circle present the constraint obtained, respectively, by [Rahmani et al. \(2012\)](#) and [Srianand et al. \(2010\)](#) based on the comparison between 21-cm and metal lines in Mg II absorbers under the assumption that α and g_p have not varied. The $\Delta\mu/\mu$ at $z < 1$ are based on ammonia and methanol inversion transitions: their 5σ errors are shown. The two measurements at $z \sim 0.89$ with larger and smaller errors are, respectively, from [Henkel et al. \(2009\)](#) and [Bagdonaite et al. \(2013\)](#) based on the same system. The two $\Delta\mu/\mu$ at $z \sim 0.684$ with larger and smaller errors are, respectively, from [Murphy et al. \(2008\)](#) and [Kanekar \(2011\)](#) based on the same system.

[King et al. \(2011\)](#) and [van Weerdenburg et al. \(2011\)](#) used H_2 and HD absorbers at $z = 2.811$ and 2.059 towards Q0528–250 and J2123–005 respectively, to find $\Delta\mu/\mu = (0.3 \pm 3.2_{\text{stat}} \pm 1.9_{\text{sys}}) \times 10^{-6}$ and $\Delta\mu/\mu = (8.5 \pm 4.2) \times 10^{-6}$. [Wendt & Molaro \(2012\)](#) and [Rahmani et al. \(2013\)](#) found $\Delta\mu/\mu = (4.3 \pm 7.2) \times 10^{-6}$ and $\Delta\mu/\mu = -(7.6 \pm 10.2) \times 10^{-6}$, using the H_2 absorber at $z = 3.025$ and 2.4018 towards Q0347–383 and HE 0027–1836.

[King et al. \(2008\)](#) find $\Delta\mu/\mu = (10.9 \pm 7.1) \times 10^{-6}$ at $z = 2.595$ towards Q0405–443. The weighted mean of these measurements and ours is of $\Delta\mu/\mu = (4.5 \pm 2.2) \times 10^{-6}$. Wavelength dependent drifts, recently reported in UVES observations, can bias the $\Delta\mu/\mu$ values to positive values. Therefore, caution should be exercised while interpreting such results as whole.

The best constraints on $\Delta\mu/\mu$ have been achieved by using NH_3 or CH_3OH absorption lines ([Murphy et al. 2008](#); [Henkel et al. 2009](#); [Kanekar 2011](#); [Bagdonaite et al. 2013](#)). Very high sensitivity of the inversion transitions associated with these molecules to $\Delta\mu/\mu$ leads to constraint of the order of 10^{-7} . The main drawback of this method is that only two systems at $z < 1$ provide the opportunity to carry out such measurements. Based on 21 cm absorption we found $\Delta\mu/\mu = 0.0 \pm 1.5$ ppm, at $z \sim 1.3$ by [Rahmani et al. \(2012\)](#), and $-(1.7 \pm 1.7)$ ppm, at $z \sim 3.2$ by [Srianand et al. \(2010\)](#). While these measurements are more stringent than those based on H_2 , we need to assume no variation of α and g_p to get a constraint on $\Delta\mu/\mu$, which is not the case in high redshift H_2 absorption systems.

A further cumulation of data on the line of sight of Q J0643–5041 would allow us to establish the actuality of partial coverage of the BLR by the H_2 -bearing cloud as well as the

possible detection of HD. However, it seems rather difficult to go much beyond our analysis on the variation of μ with UVES data. Indeed, systematic drifts in wavelength calibration over the whole blue arm of UVES can only be unveiled by absolute reference observations (of asteroids or an iodine cell, for example) in the same conditions as science observations to correct for instrumental misbehaviours. Such a systematic effect could be the origin of the preferred positive value of $\Delta\mu/\mu$ seen in this and other similar works. To shed light on the actual value of μ at high redshift, it is crucial to re-observe systems, such as the one presented here, with as much control in wavelength calibration as possible to account for systematics that escape our means in the present state of the art.

Acknowledgements. This research was supported by the Agence Nationale pour la Recherche under Prog. ANR-10-BLAN-510-01. R.S. and P.P.J. gratefully acknowledge support from the Indo-French Centre for the Promotion of Advanced Research (Centre Franco-Indien pour la Promotion de la Recherche Avancée) under contract No. 4304-2. H.R. would like to thank the Institute for research in Fundamental Sciences (IPM, Tehran) for hospitality and providing facilities during his visit in August 2013. The authors would like to thank the referee, Paolo Molaro, for useful comments and discussion.

References

- Agafonova, I. I., Molaro, P., Levshakov, S. A., & Hou, J. L. 2011, *A&A*, 529, A28
- Agafonova, I. I., Levshakov, S. A., Reimers, D., Hagen, H.-J., & Tytler, D. 2013, *A&A*, 552, A83
- Akaike, A. 1974, *IEEE Trans. Autom. Control*, 19, 716
- Bagdonaite, J., Jansen, P., Henkel, C., et al. 2013, *Science*, 339, 46
- Balashev, S. A., Ivanchik, A. V., & Varshalovich, D. A. 2010, *Astron. Lett.*, 36, 761
- Balashev, S., Petitjean, P., Ivanchik, A., et al. 2011, *MNRAS*, 418, 357
- Carswell, R. F., Becker, G. D., Jorgenson, R. A., Murphy, M. T., & Wolfe, A. M. 2012, *MNRAS*, 422, 1700
- Cartledge, S. I. B., Lauroesch, J. T., Meyer, D. M., & Sofia, U. J. 2006, *ApJ*, 641, 327
- Centurión, M., Bonifacio, P., Molaro, P., & Vladilo, G. 2000, *ApJ*, 536, 540
- Chand, H., Srianand, R., Petitjean, P., et al. 2006, *A&A*, 451, 45
- Cowie, L. L., & Songaila, A. 1995, *ApJ*, 453, 596
- Cui, J., Bechtold, J., Ge, J., & Meyer, D. M. 2005, *ApJ*, 633, 649
- Dekker, H., D’Odorico, S., Kaufer, A., Delabre, B., & Kotzłowski, H. 2000, in *SPIE Conf. Ser. 4008*, eds. M. Iye, & A. F. Moorwood, 534
- D’Odorico, S., Cristiani, S., Dekker, H., et al. 2000, in *SPIE Conf. Ser. 4005*, ed. J. Bergeron, 121
- Edlén, B. 1966, *Metrologia*, 2, 71
- Fynbo, J. P. U., Ledoux, C., Noterdaeme, P., et al. 2011, *MNRAS*, 413, 2481
- Guimarães, R., Noterdaeme, P., Petitjean, P., et al. 2012, *AJ*, 143, 147
- Henkel, C., Menten, K. M., Murphy, M. T., et al. 2009, *A&A*, 500, 725
- Hirashita, H., & Ferrara, A. 2005, *MNRAS*, 356, 1529
- Ivanchik, A., Petitjean, P., Varshalovich, D., et al. 2005, *A&A*, 440, 45
- Ivanchik, A. V., Petitjean, P., Balashev, S. A., et al. 2010, *MNRAS*, 404, 1583
- Jenkins, E. B. 2009, *ApJ*, 700, 1299
- Jorgenson, R. A., Wolfe, A. M., & Prochaska, J. X. 2010, *ApJ*, 722, 460
- Kanekar, N. 2011, *ApJ*, 728, L12
- King, J. A., Webb, J. K., Murphy, M. T., & Carswell, R. F. 2008, *Phys. Rev. Lett.*, 101, 251304
- King, J. A., Murphy, M. T., Ubachs, W., & Webb, J. K. 2011, *MNRAS*, 417, 3010
- Kulkarni, V. P., Meiring, J., Som, D., et al. 2012, *ApJ*, 749, 176
- Lacour, S., André, M. K., Sonnentrucker, P., et al. 2005, *A&A*, 430, 967
- Ledoux, C., Petitjean, P., & Srianand, R. 2003, *MNRAS*, 346, 209
- Levshakov, S. A., Dessauges-Zavadsky, M., D’Odorico, S., & Molaro, P. 2002, *MNRAS*, 333, 373
- Levshakov, S. A., Centurión, M., Molaro, P., et al. 2006, *A&A*, 449, 879
- Lodders, K. 2003, *ApJ*, 591, 1220
- Malec, A. L., Buning, R., Murphy, M. T., et al. 2010, *MNRAS*, 403, 1541
- Meshkov, V., Stolyarov, A., Ivanchik, A., & Varshalovich, D. 2006, *J. Exp. Theoret. Phys. Lett.*, 83, 303
- Mohr, P., & Taylor, B. 2000, *Rev. Mod. Phys.*, 72, 351
- Molaro, P., Levshakov, S. A., Monai, S., et al. 2008, *A&A*, 481, 559
- Murphy, M. T., Flambaum, V. V., Muller, S., & Henkel, C. 2008, *Science*, 320, 1611

- Noterdaeme, P., Ledoux, C., Petitjean, P., et al. 2007a, *A&A*, 474, 393
- Noterdaeme, P., Petitjean, P., Srianand, R., Ledoux, C., & Le Petit, F. 2007b, *A&A*, 469, 425
- Noterdaeme, P., Ledoux, C., Petitjean, P., & Srianand, R. 2008a, *A&A*, 481, 327
- Noterdaeme, P., Petitjean, P., Ledoux, C., Srianand, R., & Ivanchik, A. 2008b, *A&A*, 491, 397
- Noterdaeme, P., Petitjean, P., Ledoux, C., et al. 2010, *A&A*, 523, A80
- Noterdaeme, P., López, S., Dumont, V., et al. 2012, *A&A*, 542, L33
- Petitjean, P., Srianand, R., & Ledoux, C. 2000, *A&A*, 364, L26
- Petitjean, P., Srianand, R., & Ledoux, C. 2002, *MNRAS*, 332, 383
- Petitjean, P., Ledoux, C., Noterdaeme, P., & Srianand, R. 2006, *A&A*, 456, L9
- Pettini, M., Smith, L. J., Hunstead, R. W., & King, D. L. 1994, *ApJ*, 426, 79
- Pettini, M., Smith, L. J., King, D. L., & Hunstead, R. W. 1997, *ApJ*, 486, 665
- Pottasch, S. R., Wesselius, P. R., & van Duinen, R. J. 1979, *A&A*, 74, L15
- Prochaska, J. X., Gawiser, E., & Wolfe, A. M. 2001, *ApJ*, 552, 99
- Prochaska, J. X., Gawiser, E., Wolfe, A. M., Castro, S., & Djorgovski, S. G. 2003, *ApJ*, 595, L9
- Rafelski, M., Wolfe, A. M., Prochaska, J. X., Neeleman, M., & Mendez, A. J. 2012, *ApJ*, 755, 89
- Rahmani, H., Srianand, R., Gupta, N., et al. 2012, *MNRAS*, 425, 556
- Rahmani, H., Wendt, M., Srianand, R., et al. 2013, *MNRAS*, 435, 861
- Reinhold, E., Buning, R., Hollenstein, U., et al. 2006, *Phys. Rev. Lett.*, 96, 151101
- Roy, N., Chengalur, J. N., & Srianand, R. 2006, *MNRAS*, 365, L1
- Savage, B. D., Bohlin, R. C., Drake, J. F., & Budich, W. 1977, *ApJ*, 216, 291
- Silva, A. I., & Viegas, S. M. 2002, *MNRAS*, 329, 135
- Srianand, R., & Petitjean, P. 1998, *A&A*, 335, 33
- Srianand, R., Petitjean, P., Ledoux, C., Ferland, G., & Shaw, G. 2005a, *MNRAS*, 362, 549
- Srianand, R., Shaw, G., Ferland, G., Petitjean, P., & Ledoux, C. 2005b [[arXiv:astro-ph/0506556](https://arxiv.org/abs/astro-ph/0506556)]
- Srianand, R., Noterdaeme, P., Ledoux, C., & Petitjean, P. 2008, *A&A*, 482, L39
- Srianand, R., Gupta, N., Petitjean, P., Noterdaeme, P., & Ledoux, C. 2010, *MNRAS*, 405, 1888
- Srianand, R., Gupta, N., Petitjean, P., et al. 2012, *MNRAS*, 421, 651
- Sugiura, N. 1978, *Commun. Stat. A-Theor.*, 7, 13
- Thompson, R. I. 1975, *Astrophys. Lett.*, 16, 3
- Thompson, R. I., Bechtold, J., Black, J. H., et al. 2009, *ApJ*, 703, 1648
- Tumlinson, J., Shull, J. M., Rachford, B. L., et al. 2002, *ApJ*, 566, 857
- Tumlinson, J., Malec, A. L., Carswell, R. F., et al. 2010, *ApJ*, 718, L156
- Ubachs, W., Buning, R., Eikema, K., & Reinhold, E. 2007, *J. Mol. Spectrosc.*, 241, 155
- Uzan, J.-P. 2011, *Liv. Rev. Relat.*, 14, 2
- van Weerdenburg, F., Murphy, M. T., Malec, A. L., Kaper, L., & Ubachs, W. 2011, *Phys. Rev. Lett.*, 106, 180802
- Vanden Berk, D. E., Richards, G. T., Bauer, A., et al. 2001, *AJ*, 122, 549
- Varshalovich, D., & Levshakov, S. 1993, *JETP Lett.*, 58, 237
- Varshalovich, D. A., Ivanchik, A. V., Petitjean, P., Srianand, R., & Ledoux, C. 2001, *Astron. Lett.*, 27, 683
- Vladilo, G. 1998, *ApJ*, 493, 583
- Vladilo, G., Centurión, M., Levshakov, S. A., et al. 2006, *A&A*, 454, 151
- Weingartner, J. C., & Draine, B. T. 2001, *ApJS*, 134, 263
- Welty, D. E., Hobbs, L. M., Lauroesch, J. T., et al. 1999, *ApJS*, 124, 465
- Wendt, M., & Molaro, P. 2011, *A&A*, 526, A96
- Wendt, M., & Molaro, P. 2012, *A&A*, 541, A69
- Whitmore, J. B., Murphy, M. T., & Griest, K. 2010, *ApJ*, 723, 89
- Wolfe, A. M., Prochaska, J. X., & Gawiser, E. 2003, *ApJ*, 593, 215
- Zwaan, M. A., van der Hulst, J. M., Briggs, F. H., Verheijen, M. A. W., & Ryan-Weber, E. V. 2005, *MNRAS*, 364, 1467

Appendix A: Spectral features

We present here the spectrum bits containing some of the absorption features that were fitted for the system at $z_{\text{abs}} \approx 2.6586$. Figure A.1 shows the H I absorption with the statistical error associated with the fit represented by the shaded region. Figures A.2–A.6 show the H₂ lines ordered by J -level. Figures A.7 and A.8 show the attempt to fit HD absorptions. The results of this fit are possibly overestimating the column density and Doppler parameter. Figure A.9 shows the low-ionisation carbon features. In Fig. A.11, we present low ionisation metal absorption profiles, while Fig. A.10 shows highly ionised carbon and silicon lines.

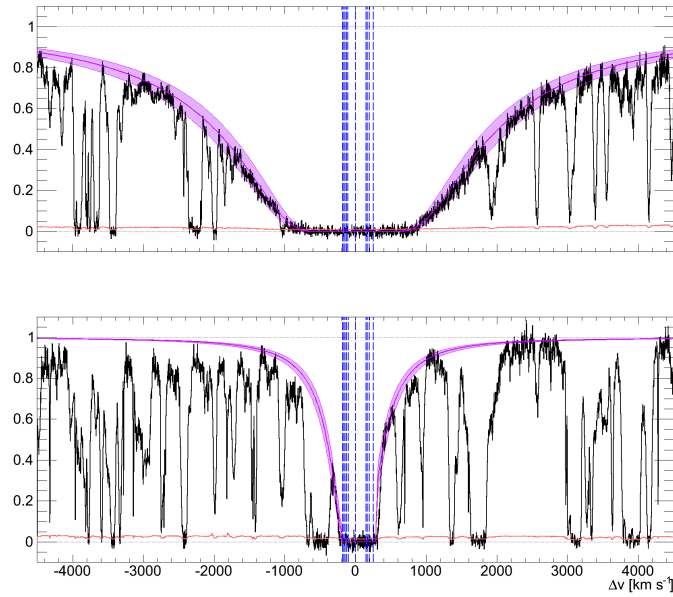


Fig. A.1. Voigt profile fits to the DLA: Lyman- α transition on *top*, Lyman- β at *lower panel*. The fit to the data with its uncertainty is shown in the shaded area. Vertical dashed lines mark the position of the H I components used for the fit, determined both from the wings of Lyman- α and Lyman- β and the profile of higher Lyman transitions. The observational error is shown at the bottom for reference.

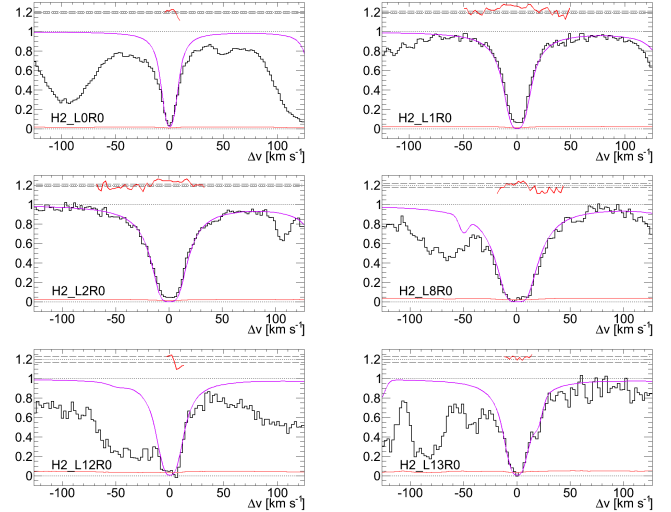


Fig. A.2. Voigt profile fits to H₂ $J = 0$. The fit to the data is represented by a line. Residuals of the fit are shown on top. The observational error is shown at the bottom for reference. Presence of residual flux is obvious in a few cases.

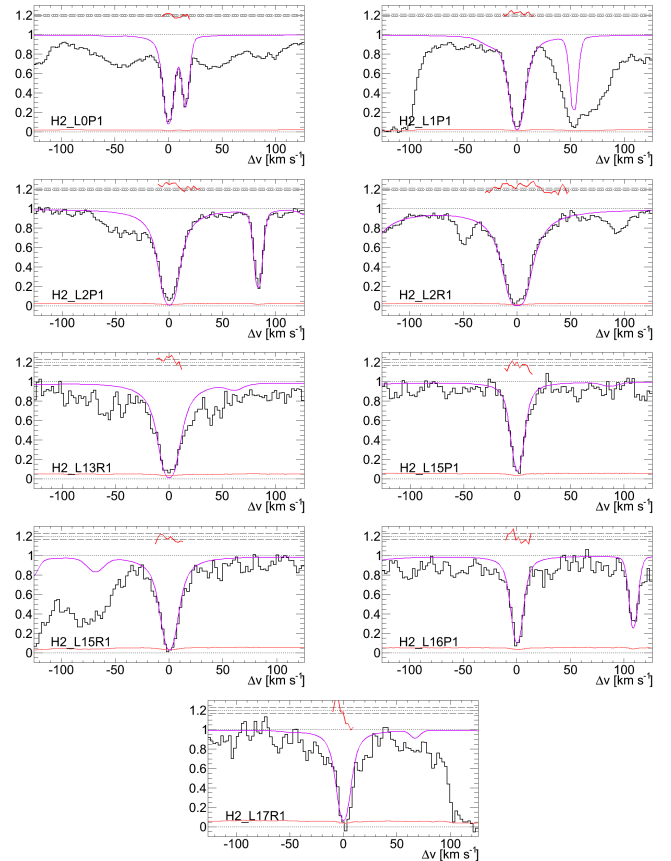


Fig. A.3. Voigt profile fits to H₂ $J = 1$. The fit to the data is represented by a line. Residuals of the fit are shown on top. The observational error is shown at the bottom for reference.

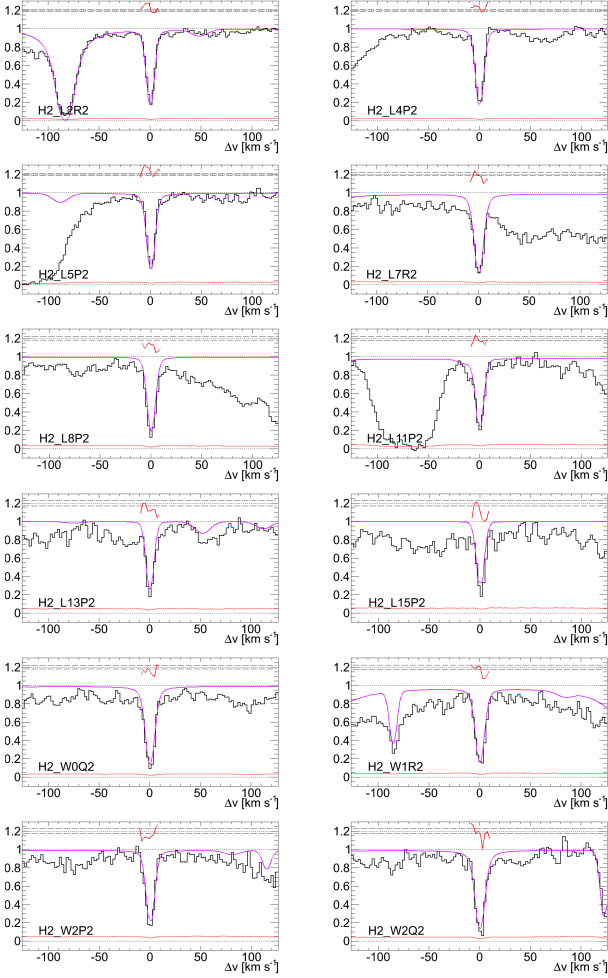


Fig. A.4. Voigt profile fits to H₂ $J = 2$. The fit to the data is represented by a line. Residuals of the fit are shown on top. The observational error is shown at the bottom for reference.

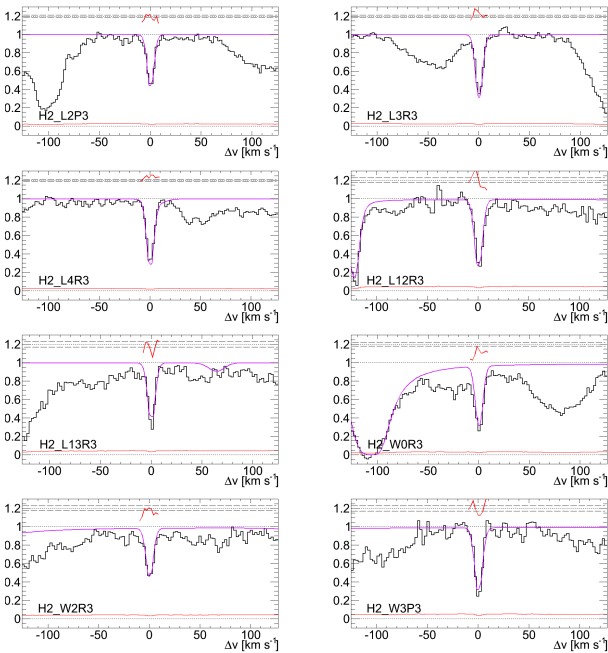


Fig. A.5. Voigt profile fits to H₂ $J = 3$. The fit to the data is represented by a line. Residuals of the fit are shown on top. The observational error is shown at the bottom for reference.

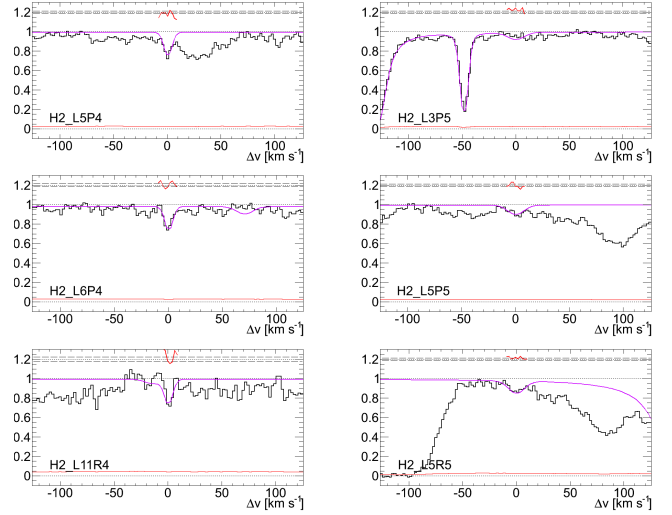


Fig. A.6. Voigt profile fits to H₂ $J = 4$ and 5. The fit to the data is represented by a line. Residuals of the fit are shown on top. The observational error is shown at the bottom for reference.

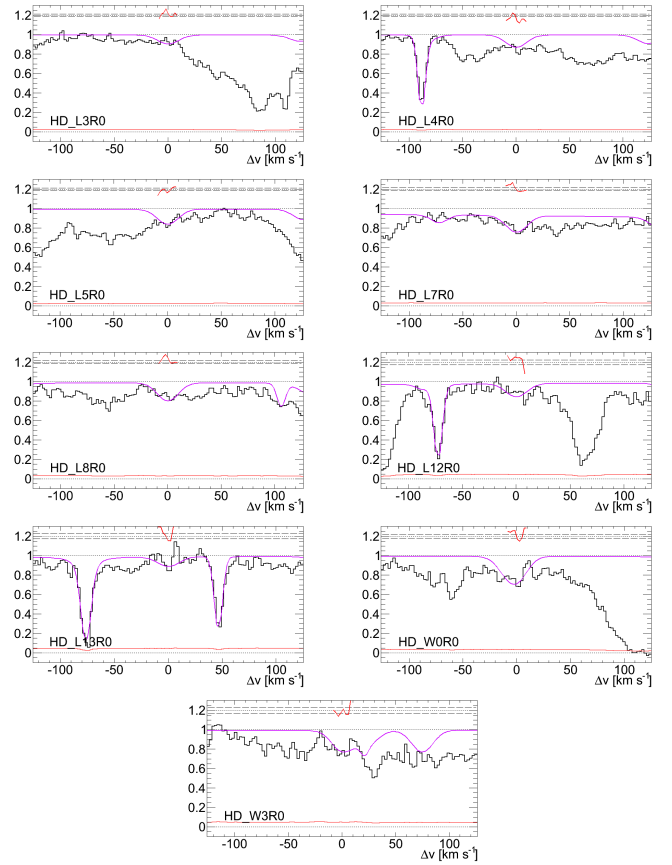


Fig. A.7. Selection of HD $J = 0$ absorption features. A tentative fit to the data is represented by a line for reference. Residuals of the fit are shown on top. The observational error is shown at the bottom for reference.

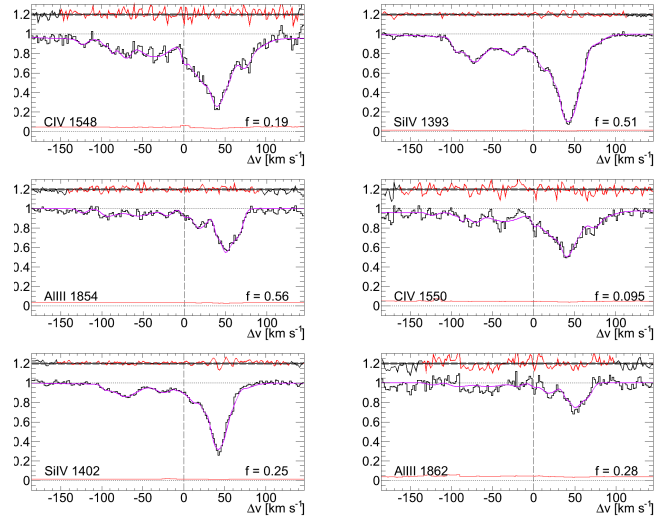
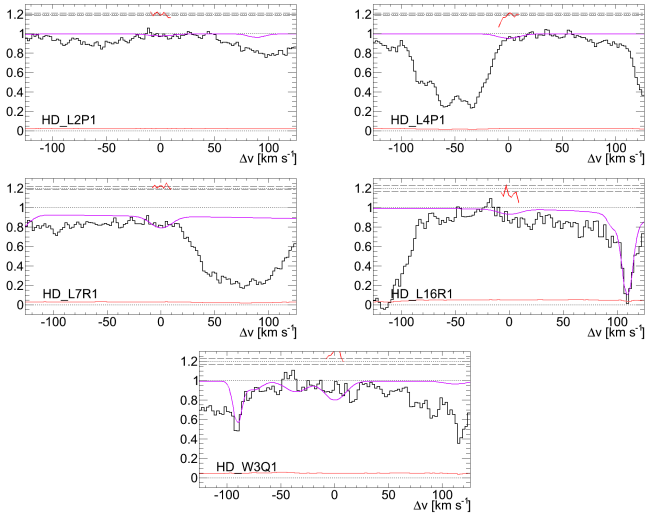


Fig. A.8. Selection of HD $J = 1$ absorption features. A tentative fit to the data is represented by a line for reference. Residuals of the fit are shown on top. The observational error is shown at the bottom for reference.

Fig. A.10. Multiple-component Voigt profile fits to high ionisation element profiles. The fit to the data is represented by a line. Residuals of the fit are shown in red on top when corresponding to the intervals used for the fit, and otherwise in black. The observational error is shown at the bottom for reference.

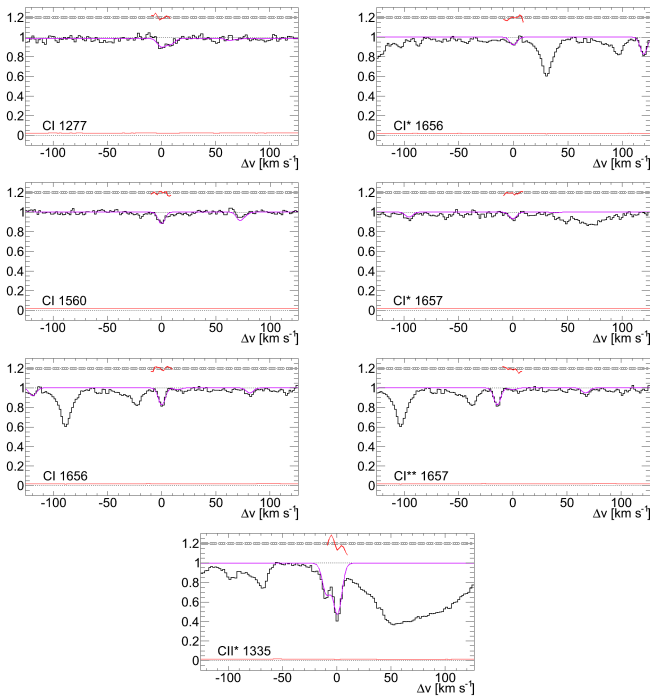


Fig. A.9. Voigt profile fits to carbon features. The fit to the data is represented by a line. Residuals of the fit are shown on top. The observational error is shown at the bottom for reference.

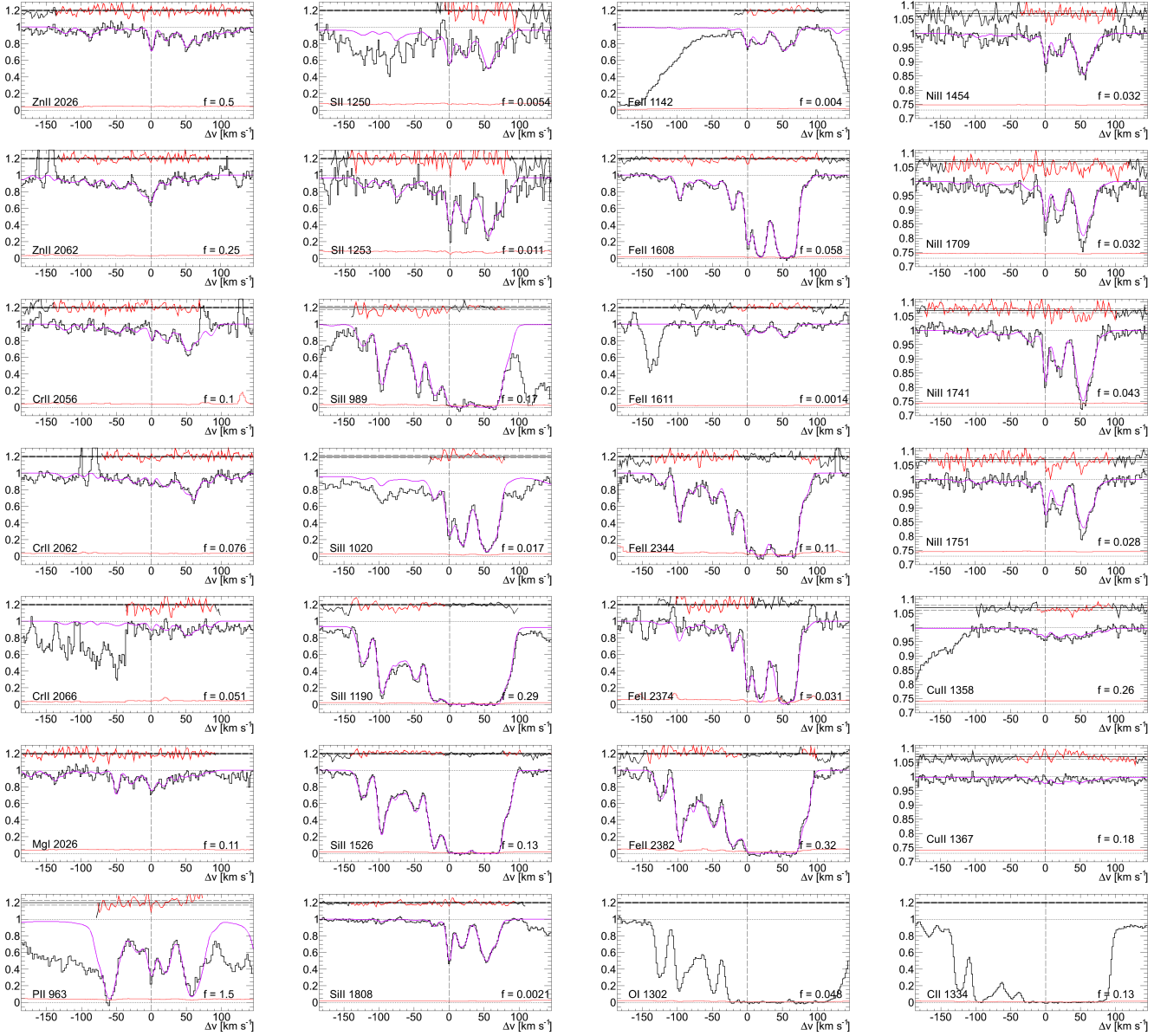


Fig. A.11. Multiple-component Voigt profile fits to low ionisation element profiles. The fit to the data is represented by a line. Residuals of the fit are shown on top, in red when corresponding to the intervals used for the fit, in black otherwise. The observational error is shown at the bottom for reference. C II and O I are impossible to decompose because all features are heavily saturated.

Appendix B: Transitions used for $\Delta\mu/\mu$ and their redshifts

We summarise in Table B.1 the H₂ lines used for the determination of $\Delta\mu/\mu$. We present the rest frame wavelength and sensitivity coefficients we used, the redshifts we have measured with a two-component model and $\Delta\mu/\mu$ included as a free parameter of the fit, as well as the velocity shift with respect to the H₂-bearing cloud redshift.

Table B.1. Laboratory wavelength of the set of H₂ transitions that are fitted along with the best redshift and errors from Vogit profile analysis. The uncontaminated (CLEAN) H₂ lines are highlighted in bold letters.

Line ID	Lab wavelength ^a (Å)	Redshift	Velocity (km s ⁻¹)	<i>K</i> coefficient ^b
L14R0	946.1693	2.658594(041)	-0.58 ± 0.34	+0.042
L10R0	981.4387	2.658604(056)	+0.19 ± 0.46	+0.041
L8R0	1001.8237	2.658601(040)	-0.06 ± 0.33	+0.035
L7R0	1012.8129	2.658591(039)	-0.86 ± 0.32	+0.031
L4R0	1049.3674	2.658585(060)	-1.32 ± 0.50	+0.017
L2R0	1077.1387	2.658602(040)	+0.09 ± 0.33	+0.006
L0R0	1108.1273	2.658600(015)	-0.12 ± 0.12	-0.008
L17R1	924.6433	2.658605(083)	+0.27 ± 0.69	+0.055
L16P1	932.2662	2.658604(035)	+0.24 ± 0.29	+0.053
L15R1	939.1242	2.658604(044)	+0.23 ± 0.36	+0.052
L15P1	939.7067	2.658606(035)	+0.37 ± 0.29	+0.051
W3Q1	947.4219	2.658607(084)	+0.46 ± 0.69	+0.021
L14P1	947.5140	2.658601(063)	-0.00 ± 0.52	+0.050
L13R1	955.0658	2.658601(055)	-0.04 ± 0.46	+0.048
L13P1	955.7082	2.658600(044)	-0.06 ± 0.37	+0.048
L12R1	963.6079	2.658598(056)	-0.27 ± 0.46	+0.046
L10P1	982.8353	2.658607(034)	+0.49 ± 0.29	+0.040
L9P1	992.8096	2.658594(043)	-0.63 ± 0.36	+0.037
L8P1	1003.2965	2.658602(029)	+0.05 ± 0.24	+0.033
L7R1	1013.4369	2.658605(030)	+0.34 ± 0.25	+0.030
L5P1	1038.1570	2.658594(021)	-0.62 ± 0.17	+0.021
L4R1	1049.9597	2.658605(030)	+0.28 ± 0.25	+0.016
L2R1	1077.6989	2.658599(021)	-0.20 ± 0.17	+0.005
L2P1	1078.9254	2.658601(018)	-0.05 ± 0.15	+0.004
L1P1	1094.0519	2.658601(019)	-0.00 ± 0.16	-0.003
L0P1	1110.0626	2.658599(017)	-0.20 ± 0.14	-0.010
L18P2	920.2432	2.658608(066)	+0.55 ± 0.55	+0.053
W4P2	932.6047	2.658608(080)	+0.55 ± 0.66	+0.026
L16R2	933.2401	2.658600(055)	-0.14 ± 0.45	+0.051
L16P2	934.1448	2.658599(053)	-0.21 ± 0.44	+0.051
L15P2	941.5992	2.658615(048)	+1.11 ± 0.40	+0.050
W3R2	947.1117	2.658606(052)	+0.39 ± 0.43	+0.023
L13R2	956.5799	2.658581(056)	-1.62 ± 0.47	+0.047
L13P2	957.6522	2.658603(029)	+0.15 ± 0.24	+0.046
L12P2	966.2754	2.658602(034)	+0.04 ± 0.28	+0.043
W2Q2	967.2811	2.658609(029)	+0.63 ± 0.24	+0.013
W2P2	968.2952	2.658594(034)	-0.58 ± 0.28	+0.012

Notes. Column (1): name of the H₂ fitted transitions. Column (2): the laboratory wavelengths. Column (3): the best-fitting redshifts for H₂ lines and their errors. Column (4): velocity offset between the redshift of a given H₂ transition and the weighted mean redshift of the all the H₂ lines. Column (5): sensitivity coefficient of H₂ lines. ^(a) Wavelengths are from Malec et al. (2010). ^(b) *K* coefficient are from Ubachs et al. (2007).

Table B.1. continued.

Line ID	Lab wavelength ^a (Å)	Redshift	Velocity (km s ⁻¹)	<i>K</i> coefficient ^b
L11P2	975.3458	2.658603(029)	+0.12 ± 0.24	+0.041
L10R2	983.5911	2.658594(039)	-0.63 ± 0.32	+0.039
L10P2	984.8640	2.658606(029)	+0.36 ± 0.24	+0.038
W1R2	986.2441	2.658607(032)	+0.50 ± 0.27	+0.006
W1P2	989.0884	2.658601(031)	-0.04 ± 0.26	+0.003
L9P2	994.8740	2.658601(032)	+0.01 ± 0.27	+0.035
L8R2	1003.9854	2.658596(021)	-0.46 ± 0.17	+0.033
L8P2	1005.3931	2.658604(022)	+0.20 ± 0.18	+0.031
W0Q2	1010.9385	2.658600(025)	-0.12 ± 0.21	-0.007
W0P2	1012.1695	2.658600(022)	-0.13 ± 0.19	-0.008
L7P2	1016.4611	2.658605(066)	+0.28 ± 0.55	+0.028
L6P2	1028.1059	2.658599(023)	-0.18 ± 0.19	+0.023
L5P2	1040.3672	2.658604(026)	+0.23 ± 0.22	+0.019
L4P2	1053.2842	2.658603(013)	+0.14 ± 0.11	+0.013
L3R2	1064.9948	2.658601(027)	-0.00 ± 0.22	+0.010
L2R2	1079.2254	2.658604(015)	+0.21 ± 0.13	+0.004
L2P2	1081.2659	2.658601(016)	-0.00 ± 0.13	+0.002
L0R2	1110.1206	2.658601(017)	-0.05 ± 0.14	-0.010
L18R3	921.7302	2.658605(083)	+0.29 ± 0.68	+0.052
L17R3	928.4374	2.658591(071)	-0.86 ± 0.59	+0.050
W4P3	934.7901	2.658591(069)	-0.85 ± 0.57	+0.023
L15R3	942.9642	2.658601(047)	-0.01 ± 0.39	+0.048
W3P3	951.6718	2.658603(039)	+0.13 ± 0.33	+0.021
L13R3	958.9466	2.658600(032)	-0.07 ± 0.27	+0.044
L13P3	960.4506	2.658607(048)	+0.51 ± 0.40	+0.043
W2R3	966.7804	2.658608(032)	+0.59 ± 0.26	+0.018
L12R3	967.6770	2.658609(026)	+0.64 ± 0.22	+0.037
W2Q3	969.0493	2.658598(087)	-0.26 ± 0.72	+0.011
L12P3	969.0898	2.658601(075)	-0.03 ± 0.62	+0.040
W2P3	970.5634	2.658602(058)	+0.03 ± 0.48	+0.010
L11P3	978.2180	2.658602(038)	+0.05 ± 0.32	+0.038
L10R3	985.9628	2.658607(047)	+0.43 ± 0.39	+0.036
L9P3	997.8271	2.658595(033)	-0.51 ± 0.28	+0.032
W0R3	1010.1303	2.658602(028)	+0.04 ± 0.23	-0.006
W0Q3	1012.6796	2.658592(044)	-0.80 ± 0.36	-0.009
W0P3	1014.5043	2.658602(028)	+0.04 ± 0.23	-0.011
L7P3	1019.5021	2.658599(040)	-0.16 ± 0.34	+0.025
L6P3	1031.1927	2.658595(035)	-0.54 ± 0.29	+0.020
L5R3	1041.1588	2.658601(029)	-0.04 ± 0.24	+0.018
L4R3	1053.9761	2.658600(019)	-0.09 ± 0.16	+0.013
L4P3	1056.4714	2.658599(018)	-0.17 ± 0.15	+0.011
L3R3	1067.4786	2.658607(022)	+0.49 ± 0.18	+0.007
L3P3	1070.1408	2.658599(027)	-0.15 ± 0.23	+0.005
L2P3	1084.5603	2.658606(020)	+0.41 ± 0.17	-0.001